Development of automatic tools for measuring acoustic glitches in seismic data of solar-type stars

Luís Filipe Regala Pereira
Mestrado em Astronomia
Departamento de Física e Astronomia
2016

Orientador
Mário João Pires Fernandes Garcia Monteiro,
Professor Associado, Faculdade de Ciências da Universidade do Porto

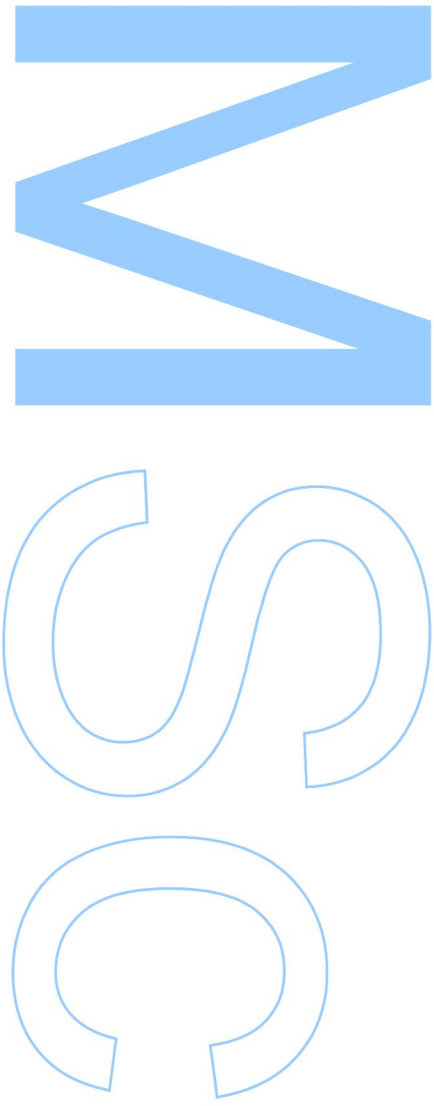

U.PORTO

FACULDADE DE CIÊNCIAS
UNIVERSIDADE DO PORTO

Todas as correções determinadas pelo júri, e só essas, foram efetuadas.

O Presidente do Júri,

Porto, / /

Acknowledgments

I would first like to thank my supervisor, Dr. Mário João Monteiro, for the all his help and guidance during this year. Having a great teacher as a supervisor significatly helps in clarifying any doubts.

I would also like to thank the support of the European Comission under the SPACEINN project (FP7-SPACE-2012-312844) and from FCT (UID/FIS/04434/2013).

To my colleagues from astronomy, especially Jota and Ana Marta, thank you for accompanying me in this unpopulated journey of being an astronomer in Portugal. To my friends Kiko, Lança, Luciano and Sara, my cousins, Américo e Carlos and my aunt Ana, thank for bothering to do some work from time to time. Your appeals to reason undoubtedly helped fight the laziness.

To my father, thank you for the enlightening discussions, even when the subjects are outside your expertise. To my sister, thank for being so calm with everything that I couldn't be bothered to get nervous either.

Finally, to my mother, a big thank you for all the support during all these years, through good and bad moments alike.

Abstract

With the increase in high precision seismic data, which started with CoRoT and Kepler and will undoubtedly continue with PLATO, it is now possible to study the internal structure of stars other than the Sun using Asteroseismology. Stellar oscillations have a lot of unique information about a star, since they are an observable probe of its inner workings. Therefore, there is great interest in the development of tools that can process that information automatically and in a robust way so as to handle the upcoming available data.

Sharp transitions in the internal stratification of a star, called acoustic glitches, give rise to a small characteristic signature in the frequencies of oscillation of a star. A variety of methods to isolate this signature from the frequencies and determine the glitches' properties already exist but they require intimate knowledge of the implementation and considerable user interaction to reach an acceptable result.

In this work two of those known methods were reimplemented with added improvements. The most important feature developed was the inclusion of an automatic pipeline of execution for the methods that requires no user interaction to perform the entire process. The improved methods were then applied for a variety of solar-like stars and the obtained results are presented and discussed.

Resumo

Com o aumento de dados sísmicos de alta qualidade, que começou com as missões CoRoT e o Kepler e que indubitavelmente continuará com a missão PLATO, é hoje possível estudar a estrutura interna de outras estrelas para além do Sol usando Asterosismologia. Oscilações estelares fornecem informação valiosa acerca das estrelas, uma vez que representam dados observáveis acerca do seu interior. Consequentemente, há um grande interesse no desenvolvimento de ferramentas que permitam processar de forma automática e robusta a quantidade de novos dados esperados.

Transições abruptas na estratificação interna das estrelas, chamadas falhas acústicas (acoustic glitches) dão origem a pequenas perturbações características nas frequências de oscilação de uma estrela. Apesar de já existirem um leque de métodos para isolar estas perturbações e determinar as propriedades das falhas, estes requerem um conhecimento profundo da implementação do método e de uam intervenção manual do utilizador para que se alcancem resultados aceitáveis.

Neste trabalho dois desses métodos já existentes são reimplementados com alguns melhoramentos, do quais se destaca a inclusão de uma pipeline de execução automática que dispensa a interação do utilizador em todo o processo. Os métodos melhorados foram aplicados a várias estrelas do tipo solar e os resultados obtidos são apresentados e discutidos.

Contents

List of Figures

List of Tables

Chapter 1

Introduction

1.1 Context

In 1926, faced with the seeming impossibility to probe behind the surface layers of a star, Eddington wondered: "What appliance can pierce through the outer layers of a star and test the conditions within?" [Eddington, 1988]. Eddington considered that the best way to understand the stellar interior was to use the laws of physics to create stellar models in which the surface was in agreement with the observed properties of the surface of the stars. Whilst this is a valid method to study stellar structure, the same Eddington warns us: "We should be unwise to trust scientific inference very far when it becomes divorced from the opportunity for observational test." [Eddington, 1988]. As such, it became necessary to find a way too 'see' inside a star. The answer would arrive some years later not through vision but through sound.

"Stars are not quiet places. They are noisy; they have sound waves in them." wrote Aerts et al. [2010]. On Earth these sound waves are better known by what they cause, the earthquakes. The scientific potential they have, however, is very similar. By studying the frequencies, amplitudes and phases of these sound waves one can infer the properties of the medium in which they were formed. This scientific application is called seismology on Earth and so, by applying the same concept on stars, one gets asteroseismology.

The reason it is possible to study the interior of a star using sound waves is because

sound waves are pressure waves. In a fluid, such as a star, they can be represented as rarefactions and compressions of the fluid propagating at the speed of sound. Stellar properties such as temperature, density, pressure or molecular weight are different throughout a star and their value defines the value of the sound speed, which in turn changes the properties of the sound waves propagating through this location that are then detected in the stellar surface. Invert the train of thought and one can grasp the information contained in the pulsations of a star. We use sound to 'see' a star's interior.

It is important to note that we can't actually measure these sound waves on Earth as they do not travel in vacuum. We can, however, measure their various effects on the star such as the periodic change in its brightness, temperature or size. Performing a frequency analysis of those periodic changes one produces the most common set of information used to asteroseismologically study a star, the power spectrum, as seen in Figure 1.1. Each frequency seen in the figure contains information about the properties of a different location inside of the star and thus, through the combined knowledge of all of them, it becomes possible to study the star's internal structure.

Besides understanding the general structure of the star, the oscillation frequencies can also contain information about specific regions in the stellar interior. Regions like the base of the convective zone and the helium second ionization zone are locations inside a star where the sound speed undergoes an abrupt variation. These locations are referred to as acoustic glitches and since the frequencies are directly related to the value of the sound speed these glitches cause perturbations to the expected values of the frequencies [Gough and Thompson, 1988; Vorontsov, 1988; Gough, 1990]. Isolating the perturbations from the frequencies allows the derivation of some of their properties, such as their locations.

As is common, the Sun was the first subject of experimentation of this new method. The oscillatory signature of its acoustic glitches has been studied extensively to determine the location of the base of the convection zone and of the second helium ionization zone [Monteiro et al., 1994; Monteiro and Thompson, 2005]. A natural follow-up to the Sun was to study solar-like stars since these share physical

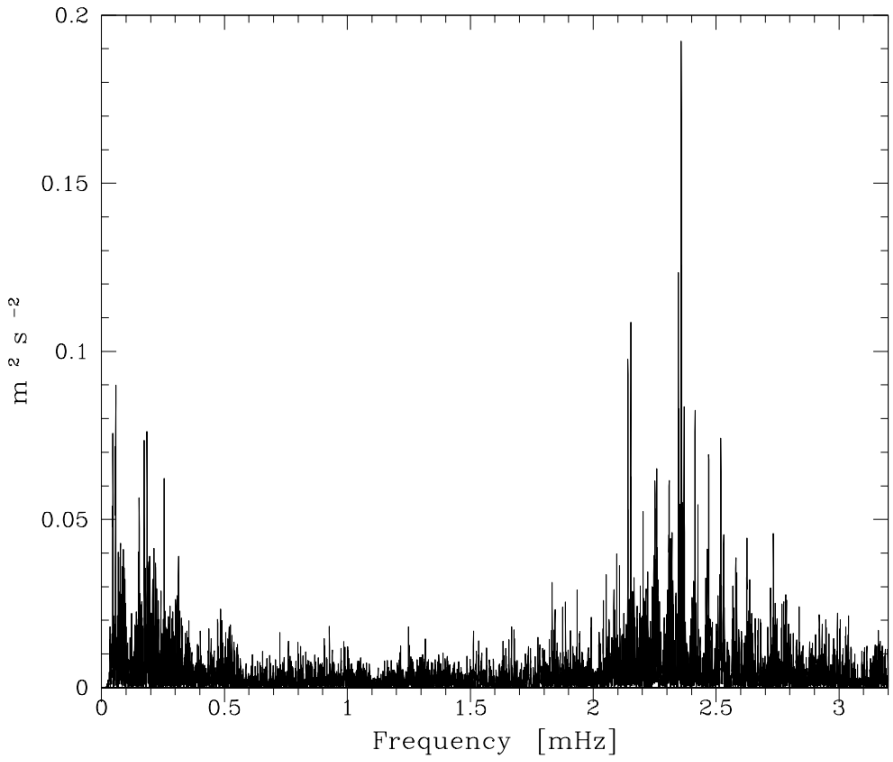

Figure 1.1: Power spectrum of α Cen A, from Bouchy and Carrier [2002]

similarities to our star. Due to the data from Kepler, these studies are now possible [Monteiro et al., 2000; Houdek and Gough, 2007; Faria, 2013; Mazumdar et al., 2014].

1.2 Motivation and Objectives

A variety of tools are available nowadays that isolate the acoustic glitches' signals and find their properties. However, most of them are not publicly distributed, in part because they are too complex and require intimate knowledge of the written code in order to achieve good results.

A main objective behind this thesis was to improve upon existing work, seeking to build a numerical procedure that is both more precise than the current methods and at the same time highly user-friendly so that it can be openly distributed. The objective would be for the tool to be capable of automatically defining all the necessary variables to achieve robust results, similar to the ones found in non-automatic tools, whilst at the same time enabling easy control to the user in case he desires to define

such variables himself.

The starting point for this thesis is the work from Faria [2013], which in turn was adapted from the work of Monteiro et al. [1994], Monteiro and Thompson [2005] and Mazumdar et al. [2012]. The influence that the various variables in each method have on the results was studied to improve the robustness of the methods and to fine tune the automatic pipeline to be implemented.

1.3 Dissertation Structure

Chapter 2 provides a physical background to explain the existence of oscillations in solar-like stars and introduces some important physical quantities. In Chapter 3, the acoustic glitches are introduced and the physical justification for their oscillatory component is derived, along with its functional form. Chapter 4 presents a detailed description of the tools developed and of the implementation of the automatic pipeline and also includes a validation of the code using solar observational data. In Chapter 5 the results obtained by applying the tools to different solar-like stars is presented and discussed. Finally, in Chapter 6 some conclusions are drawn on the work developed and possible future work is suggested.

Also important is Appendix A which describes thoroughly how to use the tools developed for this work, with descriptions on all the variables that can be controlled by the user.

Chapter 2

Theory of Stellar Oscillations

To assess the potential information contained in stellar oscillations and evaluate the best way to extract it we need to start by understanding the physical mechanisms responsible for their formation in the stars.

In this chapter we start by showing that these oscillations can be described as small perturbations in the hydrodynamic motion of a fluid. We then make some assumptions about the structure of a star to be able to perform an asymptotic analysis of the resulting solutions to further study the relation between the oscillations and the internal structure of the star.

2.1 Linear Adiabatic Oscillations

Stellar oscillations, considering adiabatic motion in a star, can be described using the principles of hydrodynamics.

In hydrodynamics it is often convenient to describe physical quantities using a Lagrangian description d/dt which is a description of the quantity following the motion of the fluid, instead of the usual Eulerian description $\partial/\partial t$, which describes the quantity from a stationary frame of reference. Both descriptions can be related by the equation

$$\frac{dy}{dt} = \frac{\partial y}{\partial t} + \vec{v} \cdot \nabla y. \tag{2.1}$$

Having the Lagrangian description, or material time derivative of a quantity, we can now write the hydrodynamical equations of a fluid. For a fluid of density ρ, with a velocity field $\vec{v} = \partial\vec{\xi}/\partial t$, pressure p and gravitational potential Φ these equations are

$$\begin{aligned} &\text{Continuity equation} && \frac{\partial \rho}{\partial t} + \nabla \cdot (\rho \vec{v}) = 0, \\ &\text{Equation of Motion} && \rho \frac{\partial \vec{v}}{\partial t} + \rho(\vec{v} \cdot \nabla)\vec{v} = -\nabla p - \rho \nabla \Phi, \\ &\text{Poisson equation} && \nabla^2 \Phi = 4\pi G \rho, \\ &\text{Adiabatic condition} && \frac{1}{p}\frac{dp}{dt} = \frac{\Gamma_1}{\rho}\frac{d\rho}{dt}, \end{aligned} \tag{2.2}$$

where Γ_1 is the first adiabatic exponent. By considering adiabatic motion in the fluid, the last equation in (2.2) is obtained by neglecting any heat exchange in the energy equation.

The previous set of equations is too difficult to solve, even numerically. However, since stellar oscillations have very small amplitudes compared with the characteristic scales of the star, these oscillations can be treated as small perturbations in a static spherically symmetric equilibrium state. In this equilibrium state all time derivatives can be neglected and all physical quantities depend only on the radial component and the Equations (2.2) can be rewritten as

$$\begin{aligned} &\vec{v} = 0, \\ &\frac{dp_0}{dr} = -\rho_0 \frac{d\Phi_0}{dr}, \\ &\frac{1}{r^2}\frac{d}{dr}\left(r^2 \frac{d\Phi_0}{dr}\right) = 4\pi G \rho_0. \end{aligned} \tag{2.3}$$

Combining the set of Equations (2.3) we can obtain the equation of hydrostatic equilibrium

$$\frac{dp_0}{dr} = -\frac{Gm\rho_0}{r^2} = \rho_0 g_0 \qquad \Longrightarrow \qquad g_0 = -\frac{d\Phi_0}{d} \tag{2.4}$$

Having defined the equilibrium state we can now perturb it by rewriting the

physical quantities

$$\rho = \rho_0 + \rho', \qquad p = p_0 + p', \qquad \vec{v} = \frac{\partial \vec{\xi}}{\partial t}, \qquad \Phi = \Phi_0 + \Phi', \tag{2.5}$$

where quantities with a superscript (') are small, time-dependant Eulerian perturbations. Replacing these new quantities in Equations (2.2) and replacing $\vec{v}$ with $\partial\vec{\xi}/\partial t$ we obtain the set of equations

$$\begin{aligned}
&\frac{\partial \rho'}{\partial t} = -\nabla \cdot \left(\rho_0 \frac{\partial \vec{\xi}}{\partial t} \right), \\
&\rho_0 \frac{\partial^2 \vec{\xi}}{\partial t^2} = -\nabla p' - \rho_0 \nabla \Phi' - \rho' \nabla \Phi_0, \\
&\nabla^2 \Phi' = 4\pi G \rho', \\
&p' + \vec{\xi} \cdot \nabla p_0 = \frac{\Gamma_{1,0} p_0}{\rho_0} (\rho' + \vec{\xi} \cdot \nabla \rho_0).
\end{aligned} \tag{2.6}$$

The perturbations added to the physical quantities are not spherically symmetric but the equilibrium state is and so the angular dependence of the perturbations can be separated from the radial one using spherical harmonics $Y_l^m(\theta, \phi)$ which are characterised by their degree l and azimuthal order m. Since we are searching for periodic solutions we search for solutions with a time dependence given by e^{iwt} where w is the oscillation frequency. We write these solutions as

$$\begin{aligned}
&\rho'(t, r, \theta, \phi) = \tilde{\rho}(r) Y_l^m(\theta, \phi) e^{iwt}, \\
&p'(t, r, \theta, \phi) = \tilde{p}(r) Y_l^m(\theta, \phi) e^{iwt}, \\
&\Phi'(t, r, \theta, \phi) = \tilde{\Phi}(r) Y_l^m(\theta, \phi) e^{iwt}, \\
&\vec{\xi} = \left[\xi_r(r), \xi_h(r) \frac{\partial}{\partial \theta}, \xi_h(r) \frac{\partial}{sin\theta \partial \phi} \right] Y_l^m(\theta, \phi) e^{iwt},
\end{aligned} \tag{2.7}$$

and then use these solutions to rewrite the set of Equations (2.6) as

$$\begin{aligned}
\frac{d\xi_r}{dr} &= -\left(\frac{2}{r} + \frac{1}{\Gamma_{1,0}p_0}\frac{dp_0}{dr}\right)\xi_r + \frac{\tilde{p}}{\rho_0 c_0^2}\left(\frac{S_l^2}{w^2} - 1\right) + \frac{l(l+1)}{w^2 r^2}\tilde{\Phi}, \\
\frac{d\tilde{p}}{dr} &= \rho_0(w^2 - N^2)\xi_2 + \frac{1}{\Gamma 1, 0 p_0}\frac{dp_0}{dr}\tilde{p} - \rho_0\frac{d\tilde{\Phi}}{dr}, \\
\frac{1}{r^2}\frac{d}{dr}\left(r^2\frac{d\tilde{\Phi}}{dr}\right) &= 4\pi G\left(\frac{\tilde{p}}{c_0^2} + \frac{\rho_0 N^2}{g_0}\xi_r\right) + \frac{l(l+1)}{r^2}\tilde{\Phi},
\end{aligned} \tag{2.8}$$

where c_0^2 is the square of the adiabatic sound speed, defined as

$$c_0^2 \equiv \frac{\Gamma_{1,0}p_0}{\rho_0}, \tag{2.9}$$

and S_l is the Lamb, or acoustic, frequency and N is the Brunt-Väisälä, or buoyancy, frequency, defined as

$$\begin{aligned}
\text{Lamb Frequency :} \qquad & S_l^2 \equiv \frac{l(l+1)c_0^2}{r^2}, \\
\text{Brunt-Väisälä Frequency :} \qquad & N^2 \equiv g_0\left(\frac{1}{\Gamma_{1,0}p_0}\frac{dp_0}{dr} - \frac{1}{\rho_0}\frac{d\rho_0}{dr}\right).
\end{aligned} \tag{2.10}$$

Equations (2.8) constitute a fourth-order system of ordinary differential equations for four dependent variables and can be solved numerically by defining four boundary conditions [Unno et al., 1989]. Analytical solutions also exist but only for very specific cases [Cox, 1980]. Note that, due to the spherical symmetry assumed for the equilibrium state, these equations are independent of the azimuthal order m.

Solutions to this set of equations exist only for discrete values of frequency. Each solution is called a mode of oscillation and has a specific frequency w_{ln}, where n is the radial order of the mode.

2.2 Asymptotic Analysis

As an alternative to the numerical solution of Eqs. (2.8) one can apply asymptotic theory to further study the equations. However, since this set of equations is of the

fourth order we first need to reduce the order of the system, which can be achieved by taking the Cowling approximation [Cowling, 1941]. This approximation states that the perturbation of the gravitational potential Φ' can be neglected if either the degree l is large or if the radial order $|n|$ is large.

By taking this approximation, the fourth order system of equations can be reduced to a second order system written as

$$\begin{aligned} \frac{d\xi_r}{dr} &= -\left(\frac{2}{r} - \frac{1}{\Gamma_{1,0}} H_p^{-1}\right)\xi_r + \frac{\tilde{p}}{\rho_0 c^2}\left(\frac{S_l^2}{w^2} - 1\right), \\ \frac{d\tilde{p}}{dr} &= \rho_0(w^2 - N^2)\xi_r - \frac{1}{\Gamma_{1,0}} H_p^{-1}\tilde{p}, \end{aligned} \tag{2.11}$$

where H_p is the pressure scale height

$$H_p = \left(-\frac{d\ln p}{dr}.\right)^{-1} \tag{2.12}$$

Then, by assuming that the oscillations vary much more rapidly than r and g, and thus neglecting derivatives of both those quantities, Eqs. (2.11) can be combined into a single second-order differential equation [Deubner and Gough, 1984]

$$\frac{d^2X}{dr^2} + \frac{1}{c^2}\left[S_l^2\left(\frac{N^2}{w^2} - 1\right) + w^2 - w_c^2\right]X = 0, \tag{2.13}$$

where we introduce the quantity X as

$$X = c^2\rho^{1/2}\nabla\xi, \tag{2.14}$$

and define the acoustic cut-off frequency, w_c, as

$$w_c^2 = \frac{c^2}{4H_\rho^2}\left(1 - 2\frac{dH_\rho}{dr}\right), \tag{2.15}$$

with H_ρ being the density scale height, analogously to Equation (2.12).

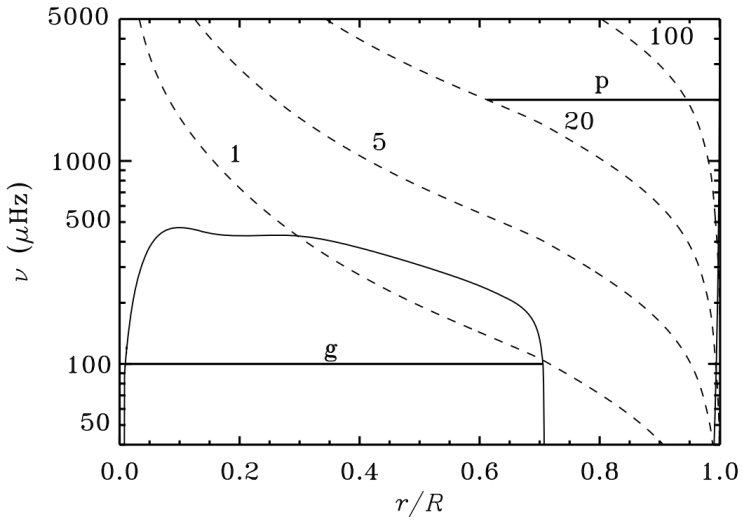

Figure 2.1: Characteristic frequencies for a model of the Sun. The buoyancy frequency N corresponds to the continuous line and the acoustic frequency corresponds to the dashed lines, labelled by the values of l. The horizontal lines indicate the trapping regions for a g mode ($\nu = 100$ μHz) and for a p mode ($l = 20$, $\nu = 100$ μHz). (Figure from Aerts et al. [2010])

Equation (2.13) can then be rewritten as a wave equation

$$\frac{d^2X}{dr^2} + K(r)X = 0, \tag{2.16}$$

with

$$K(r) = \frac{1}{c^2}\left[S_l^2\left(\frac{N^2}{w^2} - 1\right) + w^2 - w_c^2\right] \tag{2.17}$$

For $K > 0$ the solution to the wave equation is an oscillation. These waves can either be driven by pressure (p-modes) or by gravity (g-modes) and their region of propagation is determined by the characteristic frequencies S_l and N, as seen by Eq. (2.17). These characteristic frequencies are illustrated in Figure 2.1 for a solar model, along with the propagation regions of both p and g modes.

By JWKB analysis [Aerts et al., 2010, E.2] it can be found that the frequencies of oscillation satisfy the relation

$$\int_{r_1}^{r_2} K(r)^{1/2} dr \simeq \left(n - \frac{1}{2}\right)\pi, \qquad n = 1,2,\ldots\ , \tag{2.18}$$

and for acoustic oscillation modes this expression can be simplified to

$$\int_{r_t}^{R} \left(1 - \frac{S_l^2}{w^2}\right)^{1/2} \frac{dr}{c} \simeq \frac{n+\alpha}{w_{nl}}\pi, \tag{2.19}$$

where $\alpha = \alpha(w)$ is a function of frequency determined by the properties of near-surface regions [Christensen-Dalsgaard and Perez Hernandez, 1992].

For low-degree p modes the term $S_l^2/w^2 << 1$ for the majority of the range of integration and so a simple relation can be obtained for their frequencies

$$\nu_{nl} = \frac{w_{nl}}{2\pi} \simeq \left(n + \frac{l}{2} + \frac{1}{4} + \alpha\right)\Delta\nu, \tag{2.20}$$

where $\nu_{nl} = w_{nl}/2\pi$ is the cyclic frequency and

$$\Delta\nu \equiv \nu_{n+1l} - \nu_{nl} \simeq \left(2\int_0^R \frac{dr}{c}\right)^{-1} \tag{2.21}$$

is the large frequency separation, a uniform spacing in frequency between two modes with the same degree l and consecutive radial orders n that corresponds to the inverse of twice the sound travel time between the center and surface of a star.

We can also define the spacing between modes with the same value of $n + l/2$ as the small frequency separation,

$$d_{l,l+2} \equiv \nu_{nl} - \nu_{n-1l+2}. \tag{2.22}$$

These separations in the frequencies are more easily identified by looking at a frequency spectrum, such as in Figure 2.2.

Other methods to study the stellar interior consider combinations of frequencies, such as the second differences, which are the approximation to the second derivative of the frequencies and are defined as

$$\Delta_2\nu_{nl} \simeq \frac{d^2\nu}{dn^2} = \nu_{n-1l} - 2\nu_{nl} + \nu_{n+1l}. \tag{2.23}$$

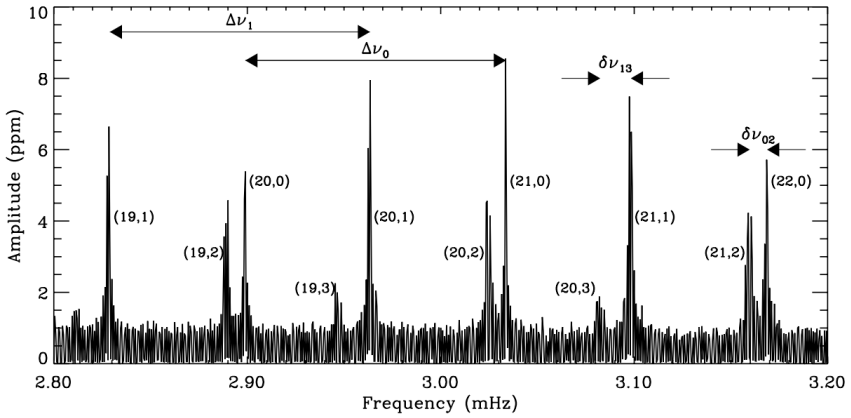

Figure 2.2: Small section of the solar amplitude spectrum showing (n,l) values for each mode. The large $(\Delta\nu)$ and small $(\delta\nu)$ separations can be easily identified.

These are a great tool to study acoustic glitches since they enhance the amplitude of the perturbation that the acoustic glitches cause in the amplitude of the oscillation modes of the star [Houdek and Gough, 2007].

Chapter 3

Acoustic Glitches

The characteristics of the oscillation modes of a star derived in the previous chapter are related to the properties of the cavity through which the sound wave is propagating. If a sharp variation in the internal structure of a star were to be located within such cavity, then that sharp variation would cause an abrupt change in the local sound speed, which in turn would cause small perturbations in the observable signal from the star. Because, ultimately, it is the change in the local sound speed that governs the value of the pressure waves properties, these sharp variations are referred to as acoustic glitches. In Figure 3.1 the glitch from the base of the convective zone can be identified when plotting the first derivative of the sound speed in respect to the acoustic depth.

The perturbation caused by each glitch is dependent on the radial order n and proportional to the amplitude of the oscillation mode at the location of the glitch (see Figure 3.2) and exhibits an oscillatory behavior when considering sequential modes of oscillation. Supposing we can isolate the glitches' components from the observable mode, it should be possible to study their properties.

In this chapter we first consider the derivation of the expressions that describe each of the signals (base of the convective zone and helium second ionization zone). Then I discuss the actual expressions used to fit the signals of both the acoustic glitches to both the oscillation frequencies and the second differences, detailing the various changes introduced.

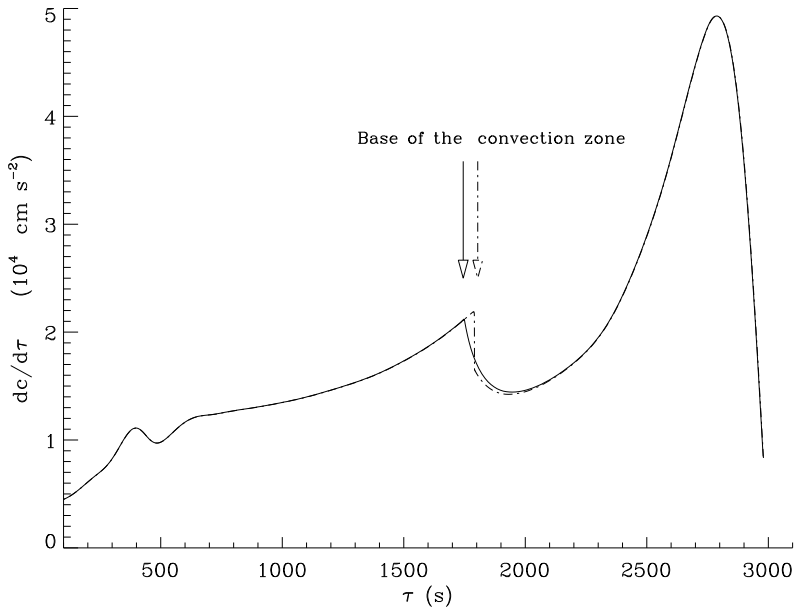

Figure 3.1: Plot of the first derivative of the sound speed in respect to the acoustic depth of a model of a solar-like star. The glitch from the base of the convective zone can be identified by the sharp change in the derivative value. The solid and dashed lines represent models without and with overshoot respectively.

3.1 Variational Analysis

The contribution from a sharp variation in the structure of a star to the frequencies can be estimated by calculating from a variational principle for the oscillation modes the effect of a localized feature.

In the case where the feature is the base of the convective zone, this sharp transition is either represented by a discontinuity in the first derivative of the sound speed, if overshoot is considered or in the second derivative, if not. Considering a variational principle for nonradial adiabatic oscillations in the Cowling approximation we can obtain the change the sharp variation causes in the frequencies, due to small perturbations in the pressure and sound speed of the star [Monteiro et al., 1994; Christensen-Dalsgaard et al., 1995]. These changes are shown to be of the form [Monteiro et al., 1994]

$$\delta w \sim A(w,l)\cos\left[2w\int_0^\tau (1-\Delta)^{1/2}\,d\tau + 2\phi\right], \tag{3.1}$$

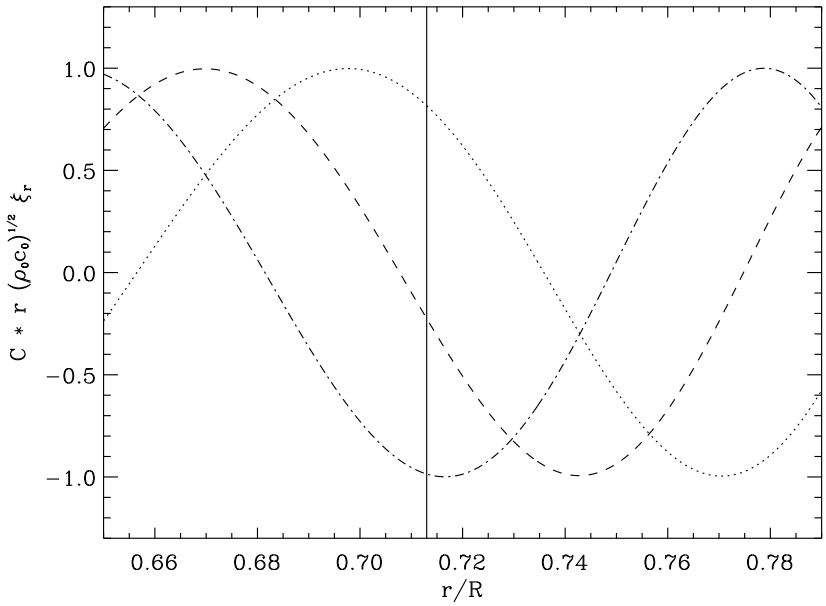

Figure 3.2: The radial amplitude of three oscillation modes of radial order $n = 14$, 15 and 16 is shown in a region of the star. The vertical line represents the location of the base of the convective zone, and the perturbation that this glitch causes in each of the frequencies is proportional to the amplitude of the mode of oscillation when it intersects the vertical line.

where τ is the acoustic depth of the glitch measured from the surface, which is defined as

$$\tau_d = \int_{r_\tau}^{R} \frac{dr}{c} \tag{3.2}$$

with c being the adiabatic sound speed, r_τ the radial distance of the glitch and R the radius of the star. Also,

$$A(w,l)_{BCZ} \sim \frac{1-2\Delta}{(1-\Delta)^2}\left[\frac{a_1}{(1-\Delta)^{1/2}}\left(\frac{1}{w}\right)^2 + a_2\left(\frac{1}{w}\right)\right], \tag{3.3}$$

with the quantity Δ defined as

$$\Delta \equiv \frac{S_l^2}{w^2} = \frac{l(l+1)c^2}{w^2 r^2}, \tag{3.4}$$

where a_1 and a_2 are constants associated with the presence of the overshoot region.

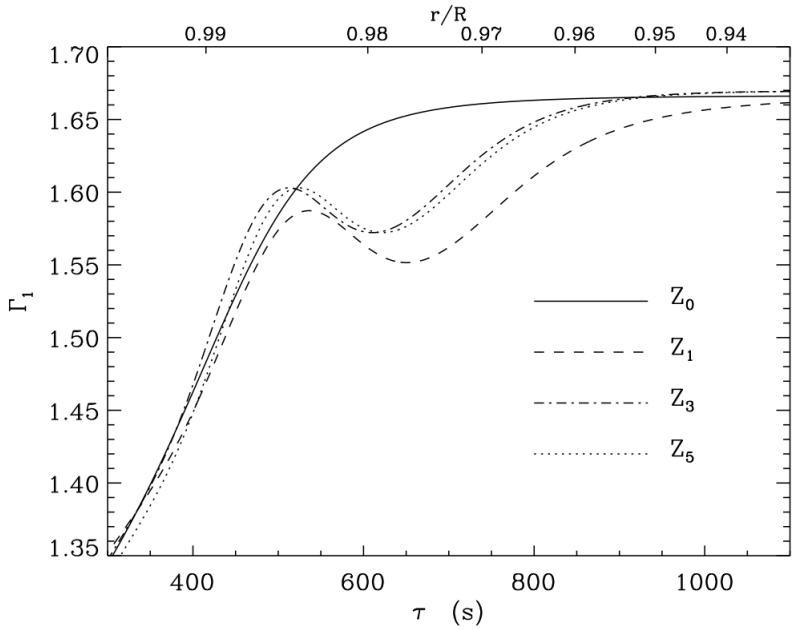

Figure 3.3: Plot of the adiabatic exponent Γ_1 for different solar models. In model Z_0 the second ionization of helium has been suppressed. The remaining models were computed using different equations of state. It is visible that the presence of the helium ionization zone causes a "bump" in the value of Γ_1. (Figure from Monteiro and Thompson [2005])

In the case where overshoot is considered, $a_1 = 0$, otherwise, $a_2 = 0$.

Because the size of the helium second ionization zone is comparable to the wavelength of the modes, describing it as a discontinuity in the sound speed is not accurate. What is considered as a sharp variation in this zone is how the ionization changes the first adiabatic exponent Γ_1 locally, producing a "bump" of about 300s as can be seen in Figure 3.3. Whilst other thermodynamical quantities are also affected in this region, the changes to the local sound speed are mainly dependent on Γ_1 and thus the contribution to the frequencies from the helium second ionization zone will be determined only by considering the changes in the first adiabatic exponent. The changes in the frequencies are shown to be of the same form as Equation (3.1) but the amplitude is of the form [Monteiro and Thompson, 2005]

$$A(w,l)_{HeII} \sim a_0 \frac{1-2\Delta/3}{(1-\Delta)^2} \frac{\sin^2\left[\beta w(1-\Delta)^{1/2}\right]}{\beta w}. \tag{3.5}$$

with the same quantity Δ as in Equation (3.4) and β being the acoustic width.

Since, for every star except the Sun, only low degree data is available, we can ignore all the dependencies on l and so we can make the approximation that $\Delta = 0$ resulting in the form of the oscillations

$$\delta w \sim A(w)\cos\left(2w\tau + 2\phi\right) \tag{3.6}$$

Each acoustic glitch will contribute to the frequencies of the star with a signal with a period of twice its acoustic depth.

The amplitudes of that signal, when considering low degree data and assuming no overshoot region, take the form of

$$\begin{aligned} A_{BCZ}(w) &\sim A_{BCZ}\left(\frac{1}{w}\right)^2, \\ A_{HeII}(w) &\sim A_{HeII}\left(\frac{1}{w}\right)\sin^2(\beta w). \end{aligned} \tag{3.7}$$

3.2 Functional form of the signals

Having all the components to describe the oscillatory signal originating from an acoustic glitch we can now write the final expressions for the signal which will be fitted to the frequencies and to the second differences. Some changes where applied to the expressions to reduce the computational complexity. First, all the frequencies were substituted with the cyclic frequency $\nu = w/2\pi$. Then, a reference value of frequency ν_r was introduced to normalize amplitudes. This value and its importance will be addressed in Chapter 4.

First we define the residuals that will be fitted as

$$\delta\nu = \nu - \nu_s = \delta\nu_{HeII} + \delta\nu_{BCZ}, \tag{3.8}$$

where ν are the observable frequencies of the star, ν_s is a smooth component that needs to be removed and will be described in detail in the next chapter and the last $\delta\nu$'s are the contributions of each of the acoustic glitches to the residuals. Following the expressions from Equations (3.6) and (3.7) and applying the previously mentioned

changes we get the expression (adapted from Monteiro et al. [1994])

$$\delta\nu_{BCZ} = A_{BCZ}\left(\frac{\nu_r}{\nu}\right)^2 \cos(4\pi\tau_{BCZ}\nu + 2\phi_{BCZ}), \tag{3.9}$$

for the contribution of the base of the convective zone , which has three free parameters A_{BCZ}, τ_{BCZ} and ϕ_{BCZ} that correspond to the amplitude, acoustic depth and phase of the signal. For the helium second ionization zone the expression is adapted from Monteiro and Thompson [2005] and has the form

$$\delta\nu_{HeII} = A_{HeII}\left(\frac{\nu_r}{\nu}\right)\sin^2(2\pi\beta_{HeII}\nu)\cos(4\pi\tau_{HeII}\nu + 2\phi_{HeII}), \tag{3.10}$$

which has four free parameters: A_{HeII}, τ_{HeII}, ϕ_{HeII} and β_{HeII} corresponding again to amplitude, acoustic depth and phase and finally, the acoustic width of the signal. Adding all the components as in Equation (3.8) we get the final function to be fitted to the frequencies

$$\begin{aligned}\delta\nu \simeq\ & A_{BCZ}\left(\frac{\nu_r}{\nu}\right)^2 \cos(4\pi\tau_{BCZ}\nu + 2\phi_{BCZ}) + \\ +\ & A_{HeII}\left(\frac{\nu_r}{\nu}\right)\sin^2(2\pi\beta_{HeII}\nu)\cos(4\pi\tau_{HeII}\nu + 2\phi_{HeII}).\end{aligned} \tag{3.11}$$

Following the same train of thought for the second differences we assume them to be of the form

$$\delta\Delta_2\nu = \Delta_2\nu - \Delta_2\nu_s = \delta\Delta_2\nu_{HeII} + \delta\Delta_2\delta\nu_{BCZ}, \tag{3.12}$$

where $\Delta_2\nu_s$ is a different smooth function that will also be described in the next chapter. The signal components from the glitches in this case are adapted from Mazumdar et al. [2014], which in turn were an adapted simplified version of the expression from Houdek and Gough [2007] and the final function is written in the form

$$\begin{aligned}\delta\Delta_2\nu \simeq\ & A^*_{BCZ}\left(\frac{\nu_r}{\nu}\right)^2 \sin(4\pi\tau_{BCZ}\nu + 2\phi_{BCZ}) + \\ +\ & A^*_{HeII}\left(\frac{\nu}{\nu_r}\right)\exp\left[-\beta^*_{HeII}\left(\frac{\nu_r}{\nu}\right)^2\right]\sin(4\pi\tau_{HeII}\nu + 2\phi_{HeII})\end{aligned} \tag{3.13}$$

which is very similar to the one for the frequencies. There are also seven free parameters: A^*_{BCZ}, τ_{BCZ} and ϕ_{BCZ} for the BCZ and A^*_{HeII}, τ_{HeII}, ϕ_{HeII} and β^*_{HeII} for the HeII.

Chapter 4

Numerical Methods

Having defined the final functions that describe the oscillatory signal that both acoustic glitches give rise to we can now describe the two numerical methods that determine the free parameters of Equations (3.11) and (3.13). Two independent but similar methods are introduced, which use either the frequencies of oscillation or the second differences as data and, after isolating the signal from the glitches by removing their respective smooth function, try to find the seven parameters that best describe the residual data.

In this chapter a detailed description of every step in each of the method's execution is given in sections 4.1, 4.2 and 4.3. Then, in section 4.4, a validation of the method using observational data from the Sun is shown. Finally, in section 4.5, the implementation of the automatic pipeline is demonstrated. Also, as mentioned beforehand, a guide on how to use the program described in this dissertation is detailed in Appendix A

4.1 Frequencies Method (Method A)

Regarding the frequencies method, hereafter Method A, the implementation consists of iteratively removing a smoothed component from the frequencies themselves and finding the parameters that best fit the residuals to Eq. (3.11) until convergence is achieved.

The smooth component is obtained separately for each degree l, by fitting a smoothing function of mode order n to the smooth frequencies [Monteiro et al., 1994]

$$\nu_{nl}^{(s)} = \nu_{nl} - \delta\nu_{nl}. \tag{4.1}$$

In the initial iteration we define $\delta\nu_{nl} = 0$ as the parameters are still unknown. The smoothing function used for each l is the polynomial

$$P_l(n) = \sum_{k=1}^{N_l} a_k^{(l)} n^{k-1}, \tag{4.2}$$

fitted to the N_l frequencies $(n,\, \nu_{nl}^{(s)})$ by minimizing

$$\sum_{i=1}^{N_l} \left(\left[P_l(n_i) - \nu_{nl}^{(s)} \right]^2 + \lambda \left(\frac{d^3 P_l}{dn^3} \right)_{n_i}^2 \right) \tag{4.3}$$

where λ is a smoothing parameter that reduces the third derivative of the polynomial. Defining a value of $\lambda = 0$ results in the polynomial interpolating all the points and all the signal being explained by the smooth function and ignoring the existence of the signal from the glitches. However, setting the value too high can also cause a lot of the smooth signal from the frequencies to not be removed, contaminating the residuals and deteriorating the fit. Thus, it is important to try and define the lowest value that still doesn't interfere with the residuals. According to Faria [2013] there is a range of values of λ where both the parameters of the fit and the their uncertainty remain approximately unchanged. In this implementation the value is chosen from within this range and takes into account the number of available points to use in the final fitting procedure.

After having determined a smooth function for every degree l we now have new values for the smooth frequencies $\nu_{nl}^{(s)}$ which we use to calculate the residuals $\nu_{nl}^{(r)} = \nu_{nl} - \nu_{nl}^{(s)}$. These are the values that will be fitted to Eq. (3.11) to determine the free parameters.

The fitting is achieved using the PIKAIA genetic algorithm [Charbonneau, 1995] which is a global minimization algorithm that utilizes concepts inspired by the pro-

cesses of evolution by natural selection. This method is especially advantageous as it doesn't require a initial guess. Instead it explores the, either automatically chosen or user-defined, interval of possible values for each of the free parameters and should, given enough time converge to global minimum in the parameter space (the implementation of the automatic pipeline that chooses the parameter interval will be discussed in section 4.5). It achieves minimization by initiating a defined number of sets of possible solutions chosen randomly from the provided interval, by default 50, and then evolving them for a given number of generations, by default 500. Each population is evaluated with a χ^2 value defined as

$$\chi^2 = \sum_l \left(\sum_n \left[\frac{\nu_{nl}^{(r)} - \delta\nu_{nl}}{\sigma_{nl}} \right]^2 \right), \tag{4.4}$$

and the population with the lowest value is chosen as the best one.

The process of removing the smooth component and finding the parameters that best fit the residuals is iteratively executed until we determine that the smooth function is perfectly characterized and thus the parameters that describe the final residuals are chosen as the correct ones. Figure 4.1 shows a diagram of the general workflow of this method.

4.2 Second Differences Method (Method B)

Unlike Method A, in the second differences method, henceforth Method B, the removal of the smooth component is only done once. After removing the smooth function we, again, find the parameters that best fit the residuals to Eq. (3.13).

In this method the smooth component is described either by a constant term or by a polynomial function,

$$P_l(n) = \sum_{k=0}^{X} c_k \nu^{-k}. \tag{4.5}$$

The choice for the form of this function depends normally on the range of second differences available but its definition is always rather arbitrary. Analogously to the

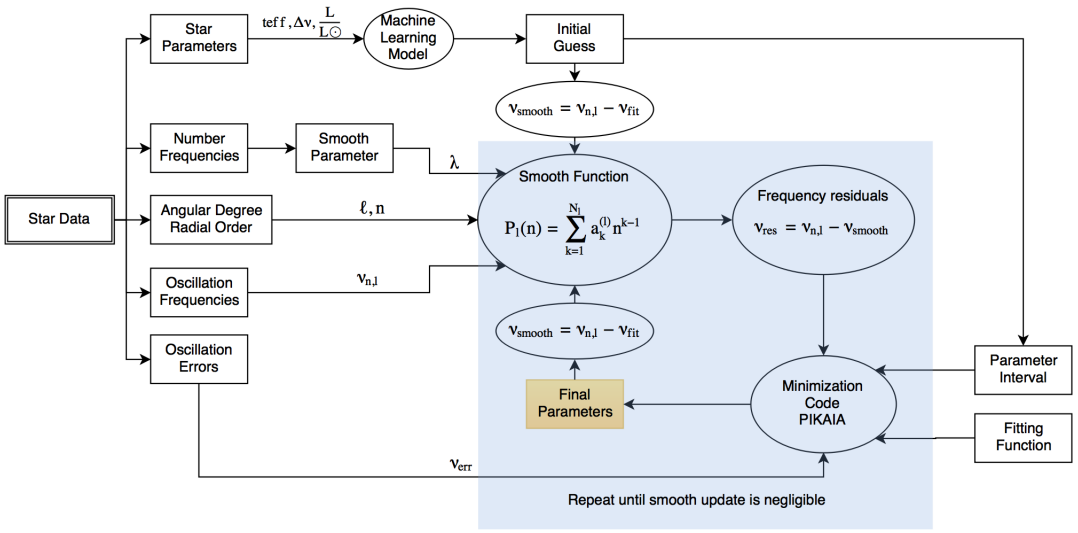

Figure 4.1: Diagram of the workflow of method A of SIGS which determines the acoustic depths of the base of the convective zone and helium II ionization zone of a star by extracting the signal caused by these glitches directly from the oscillation frequencies of the star.

procedure in the previous method we now calculate the residuals $\Delta_2\nu_{nl}^{(r)} = \Delta_2\nu_{nl} - \Delta_2\nu_{nl}^{(s)}$

The fitting procedure used in this method is exactly the same as the one used in Method A. The only difference is in the definition of the χ^2 which in this case is defined as

$$\chi^2 = \sum_l \left(\sum_n \left[\frac{\Delta_2\nu_{nl}^{(r)} - \delta\Delta_2\nu_{nl}}{\Delta_2\sigma_{nl}} \right]^2 \right). \tag{4.6}$$

A general workflow of this method is showcased in Figure 4.2

4.3 Monte Carlo Simulations

To add robustness to both methods and estimate the errors in the measurements of the parameters we perform Monte Carlo simulations. We generate alternative data sets by taking the original frequencies and changing them by a value sampled from a normal distribution with standard deviation equal to the uncertainty of the original

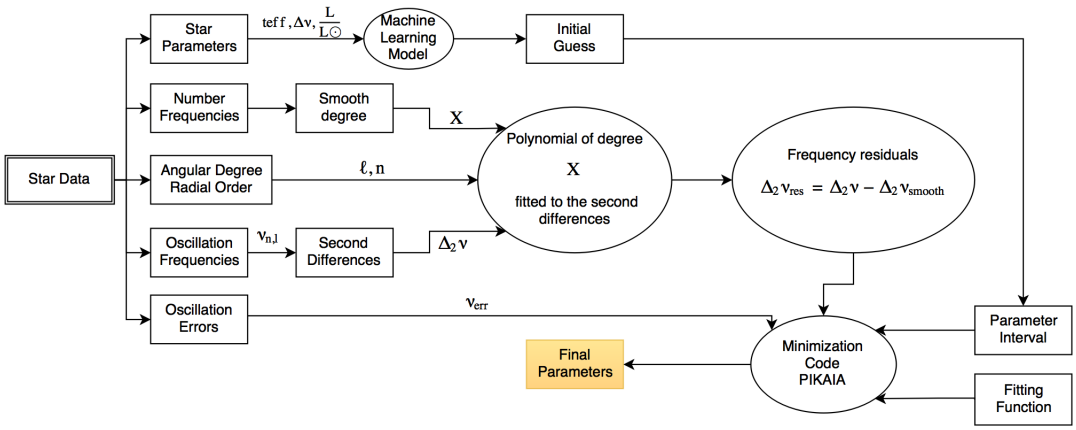

Figure 4.2: Diagram of the workflow of Method B of SIGS which determines the acoustic depths of the base of the convective zone and helium II ionization zone of a star by extracting the signal caused by these glitches from the second differences of the frequencies of the star.

frequency. To formalize, the new frequencies will be defined as

$$\nu'_{nl} = \nu_{nl} + \text{randn}(0, \sigma_{nl}), \tag{4.7}$$

where randn(x,y) is a function that generates a random number from a normal distribution of mean x and standard deviation y. The methods are then used for each of the new data sets to obtain a distribution of values for the final parameters.

4.4 Method Validation

To validate the implementations of both methods we apply them to both low-degree solar frequencies [Broomhall et al., 2009] and then compare the results with that of previous works. This validation is done without the implementation of the automatic pipeline since the results of the method will be used in the implementation of the automatic code as will be shown in the next section. As such, the interval of values for each of the parameters used was defined to be large enough to ensure the correct result is included and the population and number of evolutions was set higher than usual to increase robustness.

It is also important to note here that not all the frequencies available are used in

the methods. In the case of this validation, only frequencies with uncertainty below $0.100\mu Hz$ were considered, to improve the results obtained. In the case of other stars we could not be so severe as the uncertainties are still higher for most oscillation modes so the default value set in the program was to discard any frequencies with uncertainty above $0.500\mu Hz$.

The results obtained for both methods are summarized in Table 4.1 along with the normalized χ^2 defined as the value from Equations 4.4 and 4.6 divided by the number of points fitted. This quantity can only be used to compare results for the same star as it is dependent on some internal variables that vary with different frequencies.

Table 4.1: Comparison of the location of the Sun's acoustic glitches determined using observational data.

	This Work		Previous Works	
	$\delta\nu$	$\Delta 2\nu$	$\delta\nu$	$\Delta 2\nu$
$\tau_{BCZ}(s)$	2281.59 ± 5.00	2313.71 ± 5.32	2337	2273
$\tau_{HeII}(s)$	685.25 ± 2.94	692.29 ± 2.69	649	707
$\bar{\chi}^2_n$	0.654	35.886		

Figure 4.3 shows histograms of the results obtained for each of the glitches using Method A for 500 different sets of frequencies, as well as the mean and standard deviation of those results. Figure 4.4 shows the result of the fitting procedure for one instance of the data and the respective signal components of each of the acoustic glitches.

Similarly, for Method B, we have the histograms of the 500 realizations in Figure 4.5 and the result of the fitting for one instance of the data in Figure 4.6.

The results obtained were successful in showing that this procedure is working as intended with both precise and accurate parameters found. The interval of values for the acoustic depths where the solutions were sought was immensely larger than the most dispersed results obtained (The initial intervals were from 1500 μHz to 4500 μHz for the τ_{BCZ} and 300 μHz to 1500 μHz for the τ_{BCZ}) which shows great convergence given good enough data (the Sun obviously has the lowest observational

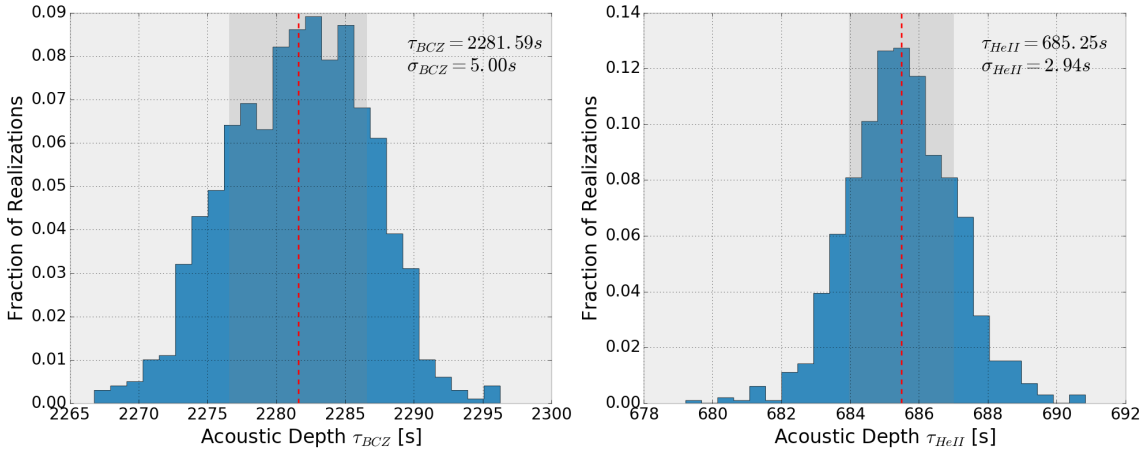

Figure 4.3: Histograms for the fitted values of τ_{BCZ} (on the left) and τ_{HeII} (on the right) obtained using Method A for 500 realizations of the frequencies of the Sun. The red dashed line represents the mean of the distribution and the grey filled area the 1σ region around the mean. Both the mean and standard deviation values are also displayed.

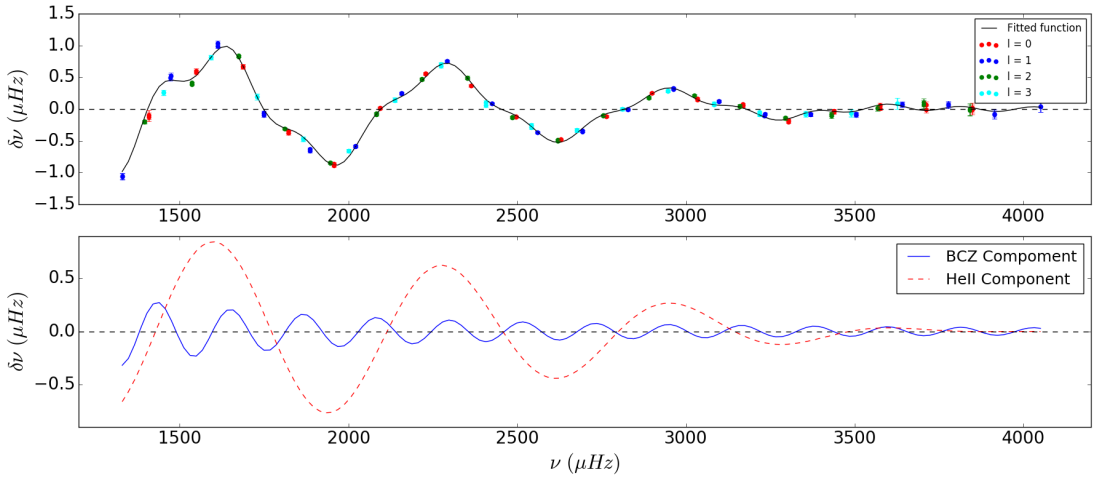

Figure 4.4: The top panel shows the fit of the residuals from the solar frequencies to Equation 3.11 using Method A. The color scheme detailed in the legend is used to differentiate between the degrees l of the frequencies. The bottom panel has the signal components from both the BCZ and HeII resulting from the fitting of the upper panel.

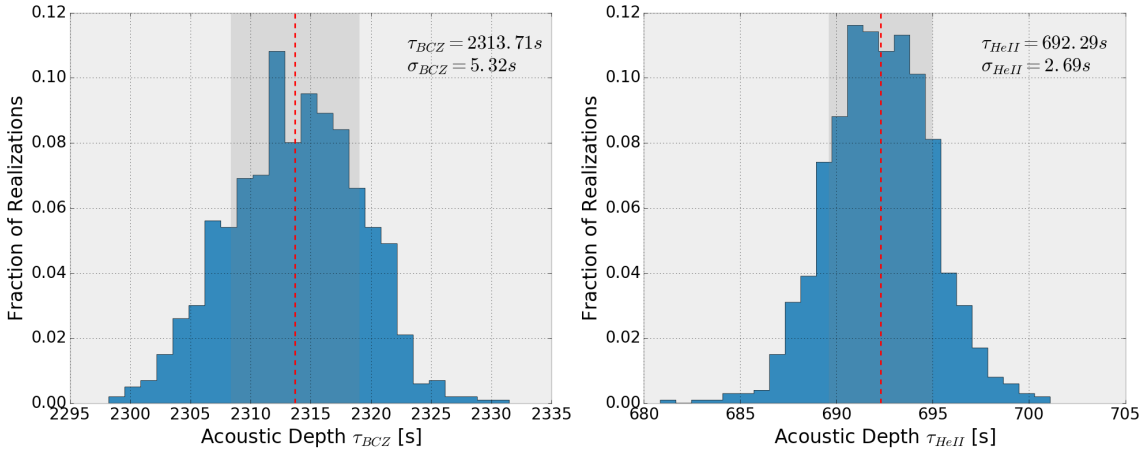

Figure 4.5: Histograms for the fitted values of τ_{BCZ} (on the left) and τ_{HeII} (on the right) obtained using Method B for 500 realizations of the frequencies of the Sun. The red dashed line represents the mean of the distribution and the grey filled area the 1σ region around the mean. Both the mean and standard deviation values are also displayed.

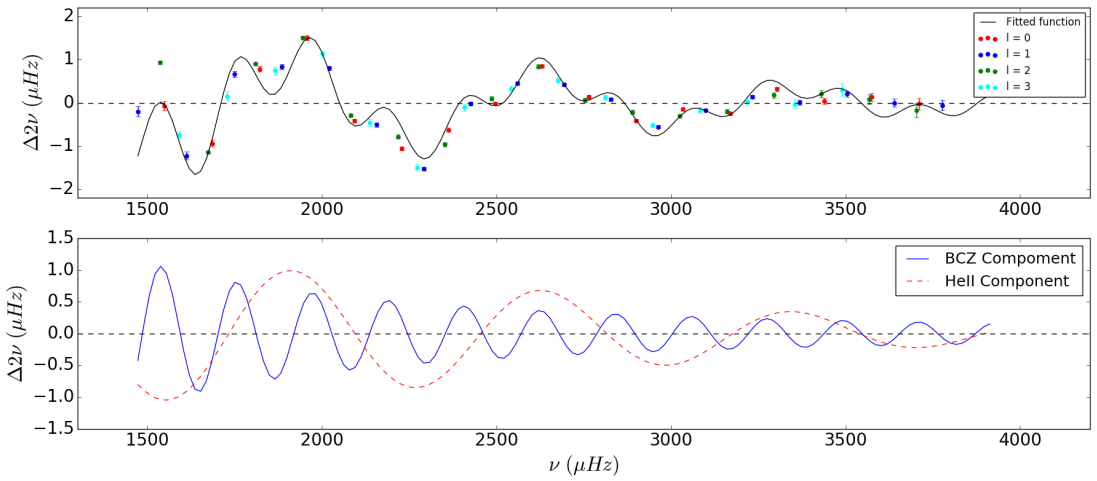

Figure 4.6: The top panel shows the fit of the second differences from the solar frequencies to Equation 3.13 using Method B. The color scheme detailed in the legend is used to differentiate between the degrees l of the second differences. The bottom panel has the signal components from both the BCZ and HeII resulting from the fitting of the upper panel.

errors associated with it's frequencies). The values obtained differ from that of other works but this is to be expected considering the different functional forms, algorithms and frequency data and selection processes used. From the values of $\bar{\chi}^2_n$ and from Figures 4.4 and 4.6 it is also noticeable that Method A is more exact in the results obtained.

4.5 Automatic Pipeline

After confirming that the method was working correctly, we applied it to a grid [Marques et al., 2008] of CESAM [Morel and Lebreton, 2008] models whose frequencies were computed using the **posc** algorithm [Monteiro, 2008].

The purpose of this application was to try and obtain a grid of results that enabled an average estimation of the values of the glitches' acoustic depths based on the stellar parameters. Since the methods developed are sensitive to the interval given to each free parameter this grid would be able to reduce the size of the interval and at the same time help identify results that show no convergence to a correct result.

The grid used considered stars with masses between $0.8M_{\odot}$ and $1.2M_{\odot}$ in intervals of $0.04M_{\odot}$ and each mass was considered with 5 different ages (1.5, 3, 4.5, 6 and 8 Gyr). Table B.1 (see Appendix B) has the results obtained for each of the models (some results didn't converge and thus were not considered or presented, to not influence negatively the following regression). An example of one of the fits done for the frequencies of a model of mass $1.0M_{\odot}$ and 4.5 Gyr is shown in Figure 4.7

The values of temperature and large frequency separation are also shown because they are the two stellar parameters that will be used to estimate the acoustic glitches' properties. This estimation is done by doing a multivariate quadratic regression to fit the effective temperature (**Teff**) and large frequency separation (**Large_sep**) values to a quadratic plane that best describes the glitch value. A regression is done separately for each glitch and the result for the glitches obtained using Method A can be seen in Figure 4.8

The functions obtained that estimate each glitch using the **Teff** and **Large_Sep**

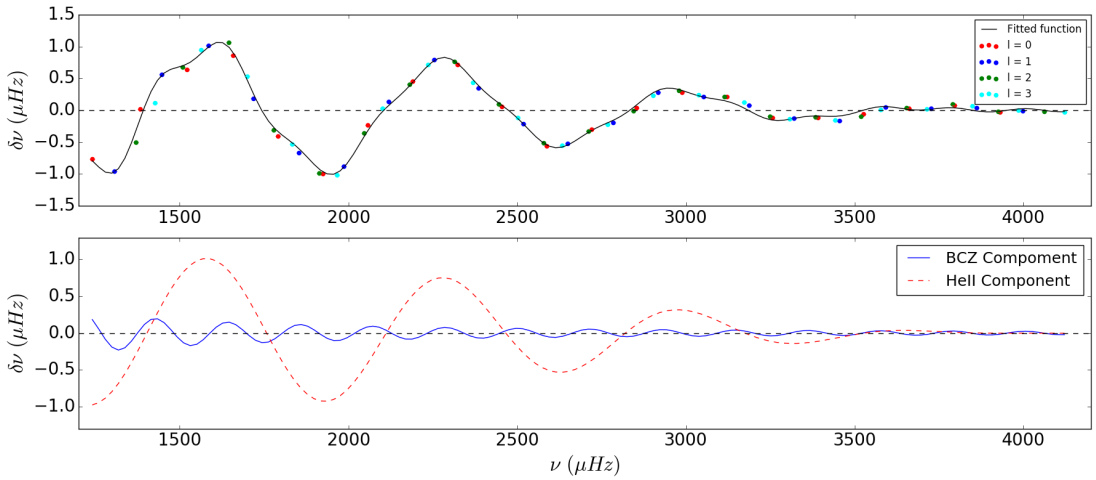

Figure 4.7: On the top panel shows the fit of the residuals from a $1.0 M_{\odot}$ and 4.5 Gyr CESAM model to Equation 3.11 using Method A. The color scheme detailed in the legend is used to differentiate between the degrees l of the frequencies. The bottom panel has the signal components from both the BCZ and HeII resulting from the fit of the upper panel.

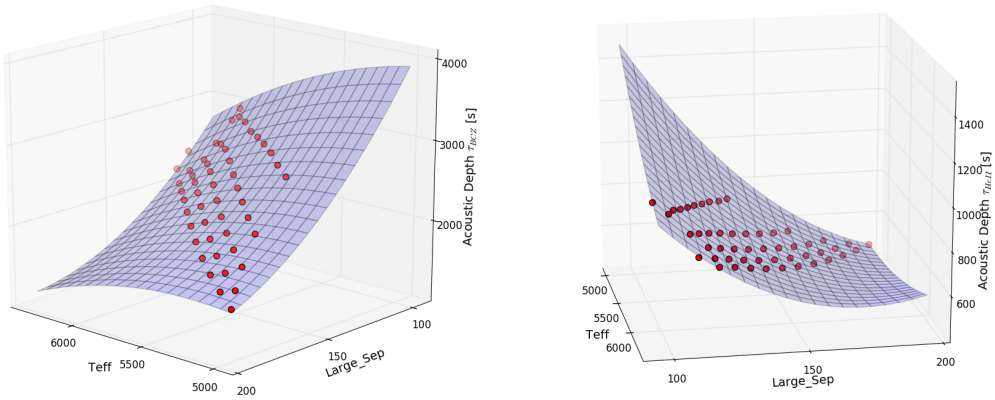

Figure 4.8: Multivariate regression applied to the values of effective temperature **Teff** and large frequency separation **Large_Sep** to the values of acoustic depth of the base of the convective zone (on the left) and the helium second ionization zone (on the right). The blue surface is the quadratic plane fitted.

values are both of the form

$$C[1] + C[2]x + C[3]y + C[4]xy + C[5]x^2 + C[6]y^2 \tag{4.8}$$

where x = **Teff** and y = **Large_Sep** and C is a vector with the six coefficients obtained from the regressions shown in Figure 4.8. These coefficients have different values for each regression and are presented in Table 4.2

Table 4.2: Values of the coefficients obtained in the regressions shown in Figure 4.8.

	τ_{BCZ}	τ_{HeII}
C[1]	3.41483132×10^{3}	1.04042545×10^{4}
C[2]	2.93091912	-1.72370361
C[3]	-8.85539759×10	-5.41870744×10
C[4]	$5.36225977 \times 10^{-3}$	$4.64983481 \times 10^{-3}$
C[5]	$-3.78731978 \times 10^{-4}$	$7.96606252 \times 10^{-5}$
C[6]	$1.32955170 \times 10^{-1}$	$7.15437626 \times 10^{-2}$

The reason this analysis was only used for the values for Method A is because all the considered results from the models were very similar between the two methods which meant that the regression would be very similar in both cases. Considering we are looking for functions that can be used to estimate the glitches' acoustic depth but still with a large degree of uncertainty, there was no need to compute separate regressions for each method.

Since we now have functions that, given the effective temperature and large frequency separation from a star, given an estimate of the values of τ_{BCZ} and τ_{HeII}, we can use these function to provide the user of the program with the possibility to try and improve their results by using these functions to automatically reduce the interval of values of the two free parameters associated with the acoustic depths of the glitches and thus improve the convergence.

Chapter 5

Results and Discussion

Having a working and validated code along with an automatic pipeline that reduces the parameter space, we can now test the program with other solar-like stars to compare its capabilities.

In the first section we apply the method to both stars from the 16 Cygni binary, Cyg A and Cyg B, and compare the results with those of Faria [2013] and Verma et al. [2014].

Then we apply the program to some stars from the work of Mazumdar et al. [2014] and compare the results. From the 19 stars present in the work, the 10 most similar to the Sun were chosen to see the results obtained.

5.1 16 Cyg A & B

The two stars from the 16 Cygni binary, 16 Cyg A and B, are a pair of solar-like stars with spectral types G1.5V and G3V respectively [Schuler et al., 2011]. Table 5.1 shows the global spectroscopic and seismic parameters [White et al., 2013] of each of the stars.

Table 5.1: Spectroscopic and seismic properties of both stars from the 16 Cygni binary, 16 Cyg A & B.

	16 Cyg A	**16 Cyg A**
m_V (mag)	5.96	6.20
T_{eff} (K)	5839 ± 42	5809 ± 39
log g	4.33 ± 0.07	4.34 ± 0.07
$[Fe/H]$	0.096 ± 0.026	0.052 ± 0.021
$\Delta\nu$ (μHz)	103.5 ± 0.1	117.0 ± 0.1
ν_{max} (μHz)	2201 ± 20	2552 ± 20

Their position in the HR diagram is shown in Figure 5.1

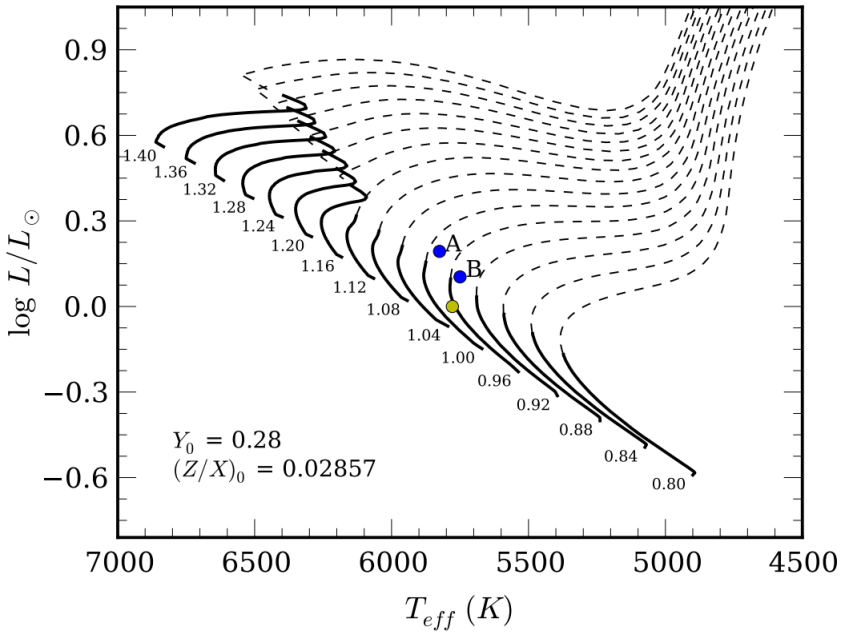

Figure 5.1: Position of the Sun (yellow circle) and 16 Cyg A and B (blue circles) on the Hertsprung-Russel diagram. The solid and dashed lines correspond to main-sequence and post main-sequence evolutionary tracks, respectively, for different masses, as indicated by the number near each track. The tracks were obtained from Marques et al. [2008]. This Figure was adapted from Faria [2013].

Using the frequencies from Verma et al. [2014] and determining the interval for the free parameters using the previously determined functions, we executed both methods for both stars.

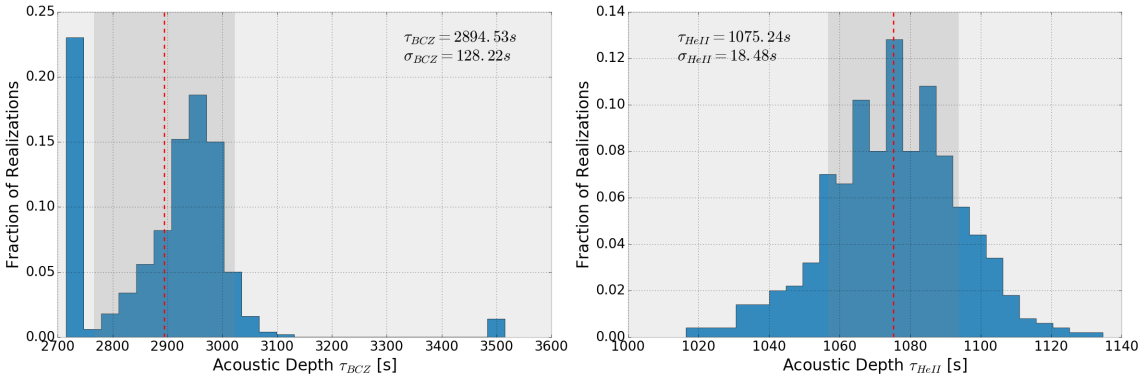

Figure 5.2: Histograms for the fitted values of τ_{BCZ} (on the left) and τ_{HeII} (on the right) obtained for 16 Cyg A using Method A.

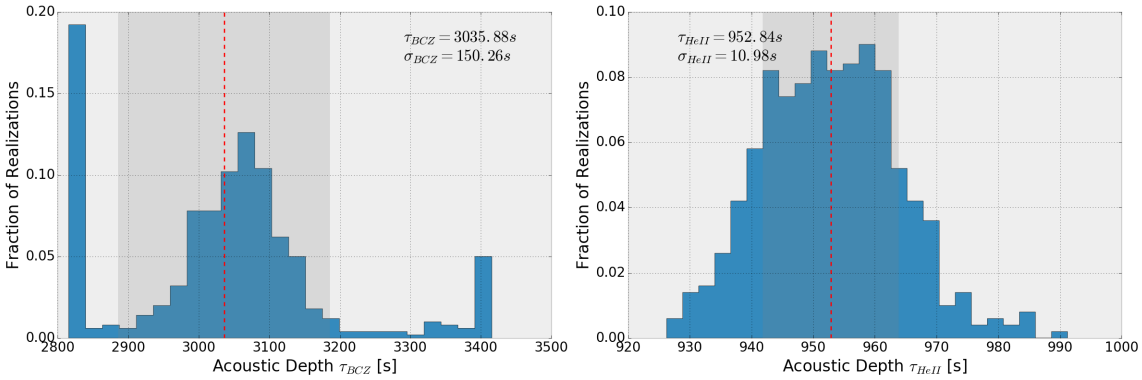

Figure 5.3: Histograms for the fitted values of τ_{BCZ} (on the left) and τ_{HeII} (on the right) obtained for 16 Cyg A using Method B.

Starting with 16 Cyg A, Figures 5.2 and 5.3 show the histograms of the results obtained for 500 realizations of the data, using Methods A and B respectively.

Figure 5.4 shows the resulting fit for both methods (frequencies on the left and second differences on the right) using one of the realizations of the data from 16 Cyg A, where the top panel has either the residuals from the frequencies fitted to Equation (3.11) or the second differences fitted to Equation (3.13) and the bottom panel has the individual components from each glitch.

Doing the same analysis for 16 Cyg B we have the histograms for both methods in Figures 5.5 and 5.6 and the fit in Figure 5.7

The resulting values from the fits are written in Tables 5.2 and 5.3 for 16 Cyg A and B, respectively.

The final results from both stars of the 16 Cygni binary are both similar between

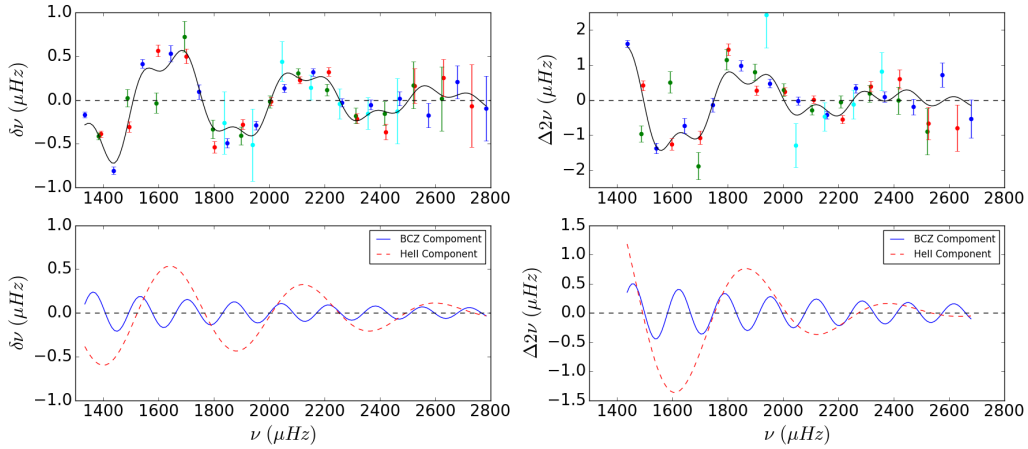

Figure 5.4: Fits obtained for Method A (on the left) and Method B (on the right) on the top and the individual components from each glitch on the bottom for 16 Cyg A.

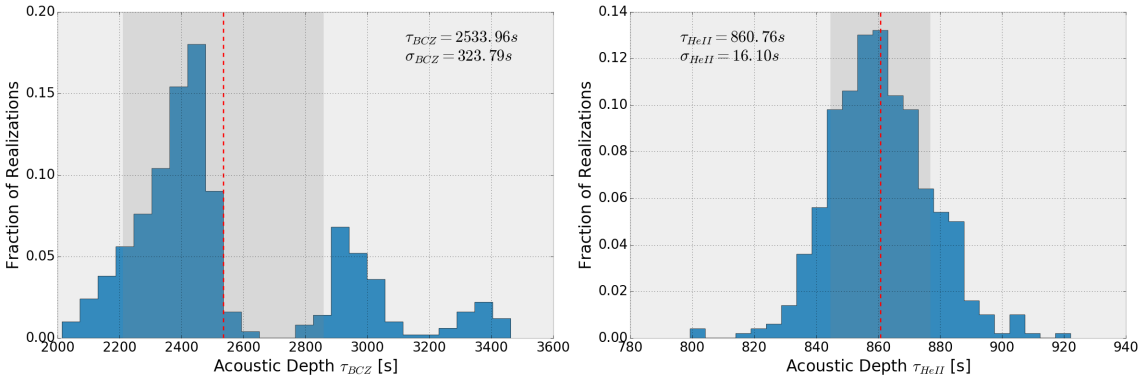

Figure 5.5: Histograms for the fitted values of τ_{BCZ} (on the left) and τ_{HeII} (on the right) obtained for 16 Cyg B using Method A.

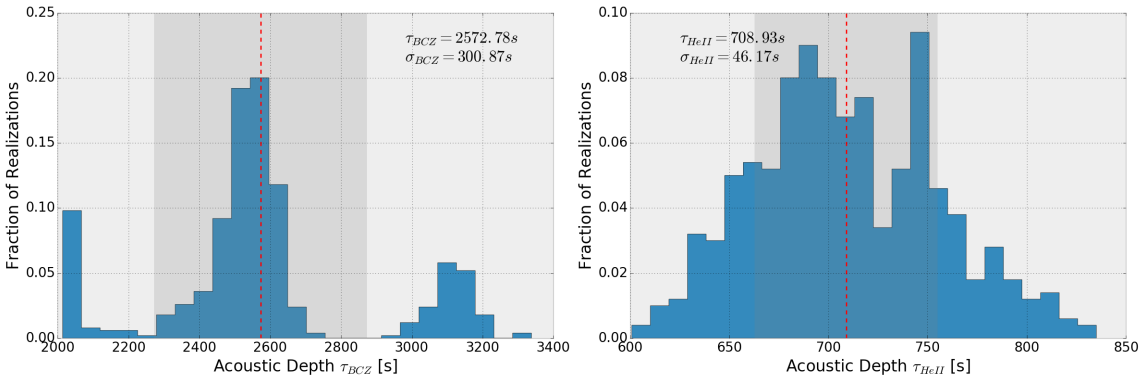

Figure 5.6: Histograms for the fitted values of τ_{BCZ} (on the left) and τ_{HeII} (on the right) obtained for 16 Cyg B using Method B.

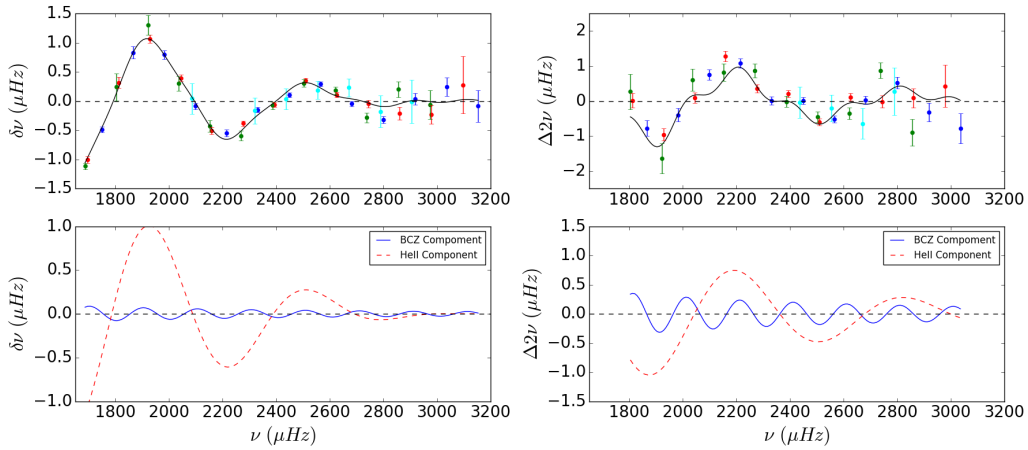

Figure 5.7: Fits obtained for Method A (on the left) and Method B (on the right) on the top and the individual components from each glitch on the bottom for 16 Cyg B.

Table 5.2: Results obtained in each method for 16 Cyg A.

16 Cyg A	Method A	Method B
$\tau_{BCZ}(s)$	2904.18 ± 88.96	3037.64 ± 147.36
$\tau_{HeII}(s)$	1178.10 ± 39.11	981.66 ± 13.33
$\bar{\chi}^2_n$	2.038	3.913

the methods and also comparing with the results from Verma et al. [2014]. The more notable differences are the value of the τ_{HeII} in Method A for Cyg A, in the right histogram of Figure 5.2, which seems to be closer to the value found in the models in the work of Verma et al. [2014] and the value of the τ_{HeII} in Method B for Cyg B, in the right histogram of Figure 5.6 which is lower than the more commonly obtained value of ∼800s.

Some differences between the methods is to be expected due to the various variables that can be tweaked. Different values in the smooth parameter in Method A or a higher degree for the smooth component in Method B are examples of constraints that can alter the final result. Despite this, it is a good indication that the program described in this work is capable of achieving similar results both for the Sun (which has a considerable higher quantity of data than the Cygni stars) and the Cygni binary compared to implementations that require user interaction to reach a valid result.

Table 5.3: Results obtained in each method for 16 Cyg B.

16 Cyg B	Method A	Method B
$\tau_{BCZ}(s)$	2538.23 ± 262.98	2451.79 ± 242.43
$\tau_{HeII}(s)$	947.26 ± 30.32	901.60 ± 30.61
$\bar{\chi}^2_n$	0.690	2.470

It is worth noting that in the 16 Cyg A histograms from Figures 5.2 & 5.3, in the figures relating to the τ_{BCZ}, the bin closest to the left margin of the histogram could be not considered since the executions that resulted in those values did not converge and could be defined as invalid. They were kept in the histogram to show the instability of these methods when there isn't enough data. Even for the Cygni stars, which have more than 40 frequencies (depends on the selection parameters) the fits lack the conclusiveness that is apparent in the Sun's histograms. From the values of $\bar{\chi}^2_n$ in Tables 5.2 and 5.3, Method A shows again to be more exact in the results provided.

5.2 Other Solar-like Stars

Finally, we apply our methods to ten solar-like stars, which were selected from Mazumdar et al. [2014]. Table 5.4 shows the global spectroscopic and seismic parameters of these stars [Basu et al., 2010; Bruntt et al., 2012]. Figure 5.8 shows the stars' position in the HR diagram.

The histograms and fits obtained for all these stars can be seen from Figure C.1 to Figure C.10 (see Appendix C).

It is clear from the figures that the results obtained are very inconsistent. In some cases there is a clear Gaussian distribution of the values with a defined mean, in other cases the program just isn't capable of converging to a valid solution and most of the results stick to one of the margins of the histogram. For these latter cases, no conclusion was drawn regarding the correct result. Table 5.5 has the results that could be determined for these ten solar-like stars.

Table 5.4: Spectroscopic and seismic properties of the ten stars selected.

KIC ID	T_{eff} (K)	log g	$[Fe/H]$	$\Delta\nu$ (μHz)
KIC008006161	5390	4.47	0.38	149.1 $\pm$ 0.1
KIC008379927	5960	4.39	-0.30	119.9 $\pm$ 0.1
KIC008760414	5787	4.33	-1.19	117.0 $\pm$ 0.1
KIC006603624	5625	4.31	0.26	109.9 $\pm$ 0.1
KIC010454113	6120	4.32	-0.07	105.1 $\pm$ 0.2
KIC006106415	5990	4.29	-0.11	103.7 $\pm$ 0.1
KIC010963065	6060	4.28	-0.21	102.4 $\pm$ 0.1
KIC006116048	5935	4.27	-0.26	100.3 $\pm$ 0.2
KIC004914923	5905	4.19	0.14	88.3 $\pm$ 0.1
KIC012009504	6065	4.21	-0.09	87.7 $\pm$ 0.1

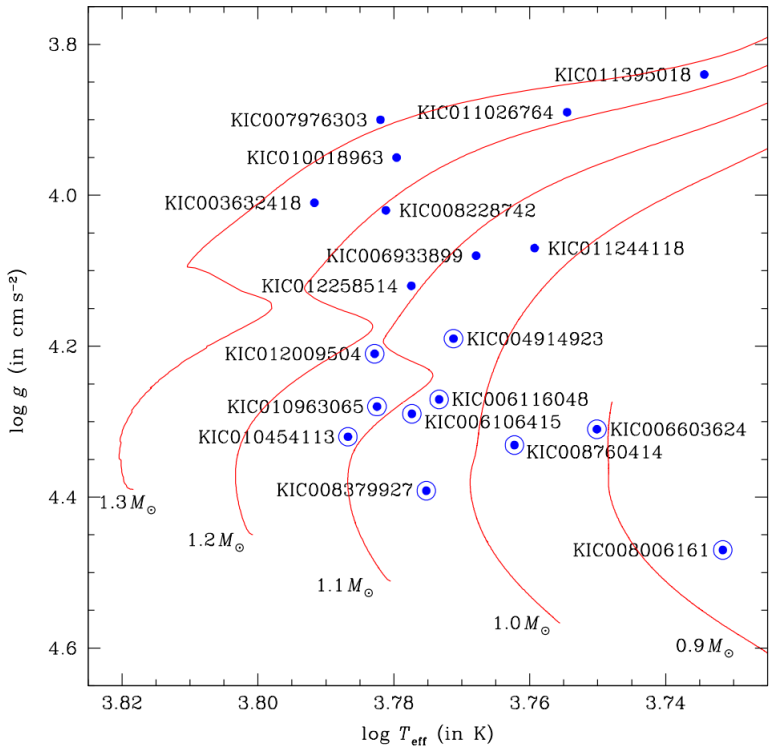

Figure 5.8: Hertsprung-Russel diagram for the 19 *Kepler* stars from Mazumdar et al. [2014]. The ten stars circled are the ones selected for this work. The red lines are evolutionary tracks with solar chemical composition and indicated mass computed with the CESAM code [Morel and Lebreton, 2008]. This Figure was adapted from Mazumdar et al. [2014].

Table 5.5: Results obtained in each method for 16 Cyg B.

	Method A		Method B	
	$\tau_{BCZ}(s)$	$\tau_{HeII}(s)$	$\tau_{BCZ}(s)$	$\tau_{HeII}(s)$
KIC008006161	2140±68.61	612.65±26.22	2233.96±50.12	—
KIC008379927	—	968.52±30.29	—	840.52±72.51
KIC008760414	—	—	—	—
KIC006603624	—	1083.66±51.83	3065.75±212.36	935.96±49.44
KIC010454113	—	837.88±9.75	2599.24±89.32	751.12±19.48
KIC006106415	—	—	—	962.53±80.31
KIC010963065	2852.93±100.45	1006.18±32.95	2791.91±138.39	1002.78±72.13
KIC006116048	—	1166.17±35.95	—	1070.51±80.38
KIC004914923	3548.15±36.44	1114.29±25.13	3561.37±54.85	—
KIC012009504	—	1138.52±28.44	—	1115.82±63.23

The lack of good results isn't unexpected considering the amount of data available for each of these solar-like stars. The number of frequencies observed for each star varies between 20 and 32 and their uncertainties are higher than the ones found in the Cygni binary. By looking at the fits from the stars it is visible that the form of the function that is being fitted is considerably different from the one for the Sun in Figure 4.4, largely due to the amount of points present. Whilst in the case of the Sun, or even the Cygni stars, we can almost draw the function using just the points, for these stars the amount of data makes the fit much more ambiguous and thus the results don't start converging to an absurd solution outside the range of defined values, which results in the bins in the margins of the histogram.

The lack of points is even more accentuated in this work compared to other methods due to our strictness in the selection of the frequencies, which was deemed necessary to improve the robustness of this method, considering it was designed to work without the user having to tweak the variables. But, whilst it could be argued that loosening this threshold might improve the results for stars with such a low amount of data, the testing performed showed that there wasn't a great improvement when allowing frequencies of higher uncertainty to be used for the fit, since the robustness

from their inclusion was directly countered by their uncertainties.

It is also expected to be more difficult to determine the values of τ_{BCZ} due to the very small amplitude of it's signal, especially compared to the signal from the helium ionization zone. Even by considering the second differences, which amplifies the amplitudes of the signals, the results are still very poor. However, as stated before, this doesn't seem to be due to the methods themselves but just due to the lack of data.

Chapter 6

Conclusions

During the realization of this work two new tools have been developed that are capable of isolating the signature of an acoustic glitch in the oscillation modes of a star and fit this signature to infer properties from the glitch, such as it's acoustic depth. One of the tools isolates the signal in the frequencies directly (Method A) and is adapted from the work found in Monteiro et al. [1994], Monteiro and Thompson [2005] and Faria [2013] whilst the second one does so in the second differences (Method B) and is adapted from the work of Houdek and Gough [2007] and Mazumdar et al. [2014]. The tools separate themselves from previous tools mentioned by being fully automatic and needing no user interaction to achieve convergence in the final result while at the same time allowing the user the possibility of tweaking the various parameters easily if they so desires. Appendix A of this dissertation was written as a guide on how to utilize the programs developed, giving a detailed description of all the user definable variables.

The presented tools, even before the implementation of the automatic pipeline, where tested with observational data from the Sun to ensure that the methods were working correctly. After that, the methods were applied to a grid of solar-like models with masses ranging from $0.8M_{\odot}$ to $1.2M_{\odot}$ in intervals of $0.04M_{\odot}$ and each mass was considered with 5 different ages (1.5, 3, 4.5, 6 and 8 Gyr) to gather a list of expected values for the acoustic depth of the glitches for different stars. This list was then used to find a function that could associate the acoustic depths of the glitches to

the effective temperature and large frequency separation of the star (Equation (4.8)). These physical quantities were the ones chosen for this function due to being the more easily obtained in stellar observations.

The functions derived in section 4.5 were then used to implement the aforementioned automatic pipeline in the tools. With this feature now present in the tools, the two stars from the 16 Cygni binary and 10 solar-like stars from the work of Mazumdar et al. [2014] were tested. For the Cygni binary the results were good and comparable to the ones found in previous works. However, for the remaining 10 stars the results are inconclusive as the lack of frequencies of oscillation leaves a lot of ambiguity in the results obtained. The signal from the helium ionization zone is clearly more easily isolated than the one from the base of the convective zone, even when considering the second differences, which can be seen from the lack of converged values for τ_{BCZ} in Table 5.5. This is to be expected since the amplitude of the signal from the BCZ is considerably smaller than the one from the HeII and, as such, is harder to detect and fit when the data has reduced quality. Nonetheless, the results are still similar to those found in preceding works which seems to indicate that the problem is not on the methods themselves or the added implementations in this work, but on the quality and quantity of data available for these stars.

To conclude, whilst the lack of a higher quantity of precise frequencies for solar-like stars seems to be the greatest hindrance to the acquisition of good results, there are still some improvements that could be attempted concerning the numerical methods themselves.

One possible idea for future development is to experiment with different or more complex functional forms for the glitches' signal. Both functional forms assumed in this work (Equations (3.11) & (3.13)) have more complex versions with additional free parameters that try to model more closely the internal structure of the star (i.e. Houdek and Gough [2007] fits the second differences to a function with 11 free parameters instead of the 7 used in this work). However, these are normally simplified, as was the case in this work, since the lack of fitting points (oscillation frequencies or second differences depending on the method) would result in poorer

fits even with a more complete functional form. Perhaps with the implementation of the automatic pipeline presented in this work which constrains the parameters space of the properties of the glitches, it might be possible to allow the inclusion of those extra free parameters to try and improve the description of the signature of the glitches. Another possibility might be to try and fit the signal from each of the glitches separately, as some methods already do, but adding the automatic pipeline present in this work to improve robustness.

Appendix A

Execution Guide

Since we have described both the numerical methods used to determine the properties of the acoustic glitches we now demonstrate how to work with each of the methods. The implementations of the methods can be obtained from their GitHub repositories

```
1 https://github.com/Fill4/sigs_freq
2 https://github.com/Fill4/sigs_diff
```

and come with a README file that has instructions on how to install the programs and the packages they depend on. In this chapter we focus on explaining how to execute and control them.

There are two ways of executing each of the programs. The first is running one of the the executables

```
1 ./sigs_freq
```

for Method A and

```
1 ./sigs_diff
```

for Method B and then pointing the program to the file with the star's oscillation frequencies when prompted. The file with the frequencies has to follow the structure shown in Listing A.1

Listing A.1: Sample of a input file for the frequencies used in the program

```
# Output from READ.PRO with the frequencies from GOLF
# Original file: GOLF_freq_5202d_dt20.dat
#   l    n         v          sig
#
     0     8    1263.3142    0.3704
     0     9    1407.4757    0.0698
     0    10    1548.3284    0.0392
     0    11    1686.5743    0.0337
     0    12    1822.1809    0.0267
```

where lines starting with # are considered comments and thus ignored and the remaining lines need to have at least the angular degree l, radial order n and frequency w, and optionally the error of the frequency observation.

The second method allows the user o run one or more files without having to point to each of them individually. This can be done by adding the relative paths of all frequency files to a single file and then running the program as

```
./sigs_freq < freqs_file
```

for example. In this case the program will run for all the files whose name is in the **freqs_file** file. Irrelevant of the execution procedure opted, the parameters determined in the fit will be written to a file called **results_freq** and **results_diff**, depending on the program.

Regarding the options available to the user, there are two occasions where the user can control some aspects of the program. The first is when calling the executable. The arguments that can be passed to the program are described in the first section of this chapter. The second way to control the execution is through the file "options_file", which can be used to define a lot of internal variables that are normally defined automatically. A sample of this file can be seen in Listing A.2

Listing A.2: Example of the structure of the option_file used in by the program.

```
&sig_bcz_controls
```

```
2       lmin = 0
3       lmax = 3
4       nlmin = 3
5       nmin = 10
6       use_error_chi2 = .TRUE.
7       ssmax = 0.300
8       degree = 0
9       pikaia_pop = 100
10      pikaia_gen = 3000
11      bcz_interval = 1000
12      he2_interval = 500
13  /
14  !Line added otherwise the code will report an error in the
      read
```

and all the variables that can be set and their usage will be described in the remaining sections.

A.1 Arguments

Arguments are commands that can be passed together with the executable at the time the executable is called. The arguments available to a user are detailed in Table A.1

An example of usage of the arguments is

```
1 ./sigs_freq -v -p < freqs_file
```

which, in this case, would execute Method A for all the filenames in **freqs_file** and during execution would print all the information of what is doing to the terminal (-v command) and in the end show plots of the results obtained (-p command).

Table A.1: List of all the arguments that can be passed with the program's executable.

Argument	Description
-h or - -help	Shows a help menu and stops the program. This menu also has a list and small description of all available arguments and small instructions on how to use the program.
-v or - -verbose	Allows the program to show information in the shell during execution.
-p or - -plots	Shows plots of the results at the end of execution.
-a or - -auto	Informs the program to determine all parameters automatically by reading the star parameters from the frequency file. The star's temperature needs to be provided in the first line of the file.

A.2 Input Data

Before performing any of the methods, both of the programs need to read the oscillation frequencies (the second differences are determined using these) from the provided files and select the ones that fulfill all the defined constraints. These constraints, that can be changed by the user by defining them in the options file, are described in Table A.2

A.3 Smooth Removal

The next step in each method is the removal of the smooth parameter. In the case of the frequencies there are two variables that can be changed, **lambda** and **smooth_iter_max** and for the second differences there is only one variable **degree**. Their descriptions can be seen in Table A.3

A.4 Minimization

After removing the smooth component from the data both programs run the minimization algorithm that will try to find the parameters that best fit the residuals to

Table A.2: List of all the variables that are available to control the selection of the frequencies in both the programs.

Variable	Description
lmin	Minimum value accepted for the degree of the frequencies.
lmax	Maximum value accepted for the degree of the frequencies.
nmin	Minimum value accepted for the radial order of the frequencies.
nmax	Maximum value accepted for the radial order of the frequencies.
nlmin	Minimum number of radial modes for a degree l. If this number is not reached none of the frequencies of that degree will be considered.
use_error_chi2	Defines if the program should consider the errors of the frequencies both in the selection and the minimization processes. The possible values are .TRUE. and .FALSE.
ssmax	Maximum value accepted for the error of a frequency. Only applied if use_error_chi2 is defined as .TRUE. . Default value is set to 0.5 μHz.

the functions described in section 3.2. The minimization method used is the PIKAIA genetic algorithm which has two variables that can be controlled by the user, which are described in Table A.4

Defining higher values for any of the two variables will improve the minimization procedure but will also increase the execution time so a balance should be struck. The default values defined were 80 and 3000 respectively.

We need to also constrain the interval of values in which the minimization algorithm will search each of the free parameters. Whilst the amplitude, phase and β parameters are all well constrained, the values for the location of the glitches are more difficult to define and if the user wants to control this interval, it is possible by using the variables in Table A.5

Finally, the last variable that can be set in the file is the reference frequency value **w0ref**, which is used to normalize the frequencies for the fitting. The value set for this quantity is by default the value of the frequency for the angular degree $l = 0$ and for the radial order $n = 18$. If this frequency is not available the program will use

Table A.3: List of all the variables that are available to control the form of the smooth functions in both of the methods.

Variable	Description
lambda	Smoothing parameter that controls how much Equation 4.2 follows the frequencies. This value is expected to be between 10^{-4} and 10^{-7} [Faria, 2013], depending on the number of selected frequencies.
smooth_iter_max	Maximum number of iterations performed in Method A to describe the smooth function and determine the free parameters. Values above 5 are not recommended.
degree	Degree of the polynomial from Equation 4.5 that will be removed from the second differences. Selecting a value of 0 will make the program use the median of the data and values above 3 are normally not expected.

the mean of the available frequencies though this choice is not the ideal.

Table A.4: List of all the variables that are available to control the execution of the minimization algorithm PIKAIA.

Variable	Description
pikaia_pop	Size of the population of individuals generated by the algorithm. Each subject in the population is a set of 7 free parameters that are initialize randomly from the considered interval.
pikaia_gen	Number of generations for which the population is evolved in the algorithm. At the end of evolution the subject from the population with the best parameters (according to either Equation 4.4 or 4.6 depending on the method).

Table A.5: List of all the variables that are available to control the execution of the minimization algorithm PIKAIA.

Variable	**Description**
upper_tau_bcz	Upper limit for the value of the BCZ glitch.
lower_tau_bcz	Lower limit for the value of the BCZ glitch.
upper_tau_he2	Upper limit for the value of the HeII glitch.
lower_tau_he2	Lower limit for the value of the HeII glitch.

Appendix B

Regression Data

Table B.1: Values for the acoustic depth of the glicthes from the base of the convective zone (BCZ) and the helium second ionization zone (HeII) obtained for the various models introduced in section 4.5 using the frequencies method (3^{rd} and 4^{th} columns) and using the second differences method (5^{th} and 6^{th} columns) in relation to the values of effective temperature (Teff) and large separation of frequencies. It is noticeable that the values from both methods are very similar.

Teff (K)	Large_Sep (μHz)	τ_{BCZ} Freq (s)	τ_{HeII} Freq (s)	τ_{BCZ} Diff (s)	τ_{HeII} Diff (s)
4970.135	195.320	1652.650	462.172	1654.532	489.110
5066.247	185.560	1754.261	496.194	1757.760	524.510
5168.783	173.695	1900.580	545.560	1900.974	565.915
5274.918	158.016	2138.902	629.856	2135.595	618.007
5373.200	132.768	2623.482	823.396	2657.439	741.974
5146.274	187.345	1712.497	484.433	1713.935	509.486
5236.309	177.457	1820.951	521.772	1824.750	549.209
5328.323	165.612	1974.083	574.572	1977.081	596.441
5417.055	150.446	2221.244	661.274	2215.467	651.367
5485.511	128.261	2691.113	843.674	2709.389	768.014
5314.037	179.395	1776.013	507.494	1778.025	530.645
5397.309	169.345	1892.146	549.132	1898.010	575.422
5477.200	157.589	2052.267	605.986	2057.846	627.866
5548.348	143.122	2303.992	694.452	2296.876	685.723
5591.344	123.382	2768.451	867.857	2766.003	797.354
5471.506	171.414	1844.180	531.739	1846.349	553.094
5546.562	161.300	1973.207	577.622	1976.443	602.573
5613.409	149.793	2137.817	638.995	2144.469	661.310
5667.483	136.295	2379.630	728.474	2374.520	721.010

5691.438	119.353	2811.753	884.441	2789.742	818.542
5620.718	163.380	1918.002	557.772	1917.753	577.644
5685.766	153.284	2058.739	607.272	2059.737	631.512
5739.677	142.233	2231.945	672.703	2236.266	695.489
5778.502	129.828	2455.790	761.335	2458.122	759.888
5786.187	115.338	2834.948	903.182	2803.140	838.610
5759.525	155.347	1991.912	586.207	1987.927	604.774
5814.763	145.434	2143.669	638.554	2139.087	661.738
5857.948	134.963	2327.877	705.638	2325.249	727.303
5880.683	123.931	2547.436	793.488	2560.422	796.584
5877.763	111.835	2845.266	918.348	2808.882	862.003
5888.404	147.456	2056.164	617.453	2053.548	634.070
5935.191	137.853	2213.663	672.146	2207.382	694.193
5967.086	128.165	2402.407	738.955	2394.124	760.867
5978.964	118.604	2621.751	821.136	2621.763	826.109
5965.725	108.158	2909.135	933.562	2940.332	893.896
6010.034	139.726	2100.528	651.888	2108.358	664.111
6047.626	130.697	2244.432	707.203	2253.109	725.002
6069.333	121.828	2416.315	772.872	2424.209	793.190
6071.313	113.853	2617.952	845.736	2621.838	859.562
6052.232	104.580	2914.419	952.870	2929.476	927.509
6124.835	132.376	2109.373	688.944	2125.567	694.579
6152.824	123.963	2241.950	744.043	2261.803	756.806
6166.715	116.143	2391.822	804.931	2414.065	822.787
6160.684	109.577	2565.230	868.294	2581.586	884.650
6137.858	101.936	2821.967	957.502	2832.442	958.214
6236.328	125.100	2111.920	727.733	2151.638	724.805
6255.695	117.525	2223.225	777.150	2282.793	784.997
6155.813	95.934	2931.268	1017.619	2957.067	1014.331
6344.335	118.110	2208.113	760.195	2184.570	748.879
6355.804	110.433	2385.511	812.261	2331.119	813.593

Appendix C

Figures for Solar-like Stars

In this Appendix the results obtained for the 10 solar-like stars from Mazumdar et al. [2014] are presented. Each figure has three plots. The first two are histograms with the results obtained for the acoustic depths of the base of the convective zone (on the left) and helium second ionization zone (on the right) for Method A (top plot) and Method B (middle plot). The bottom plot is formed by 4 subplots. The top subplots show the fit of the residuals to Equation (3.11) using Method A (on the left) and the second differences to Equation (3.13) using Method B (on the right). The color code is used to separate points of different angular degree l where red is $l = 0$, blue is $l = 1$ and green is $l = 2$. The bottom subplots show the separated components from each of the glitches obtained from the fit directly above it.

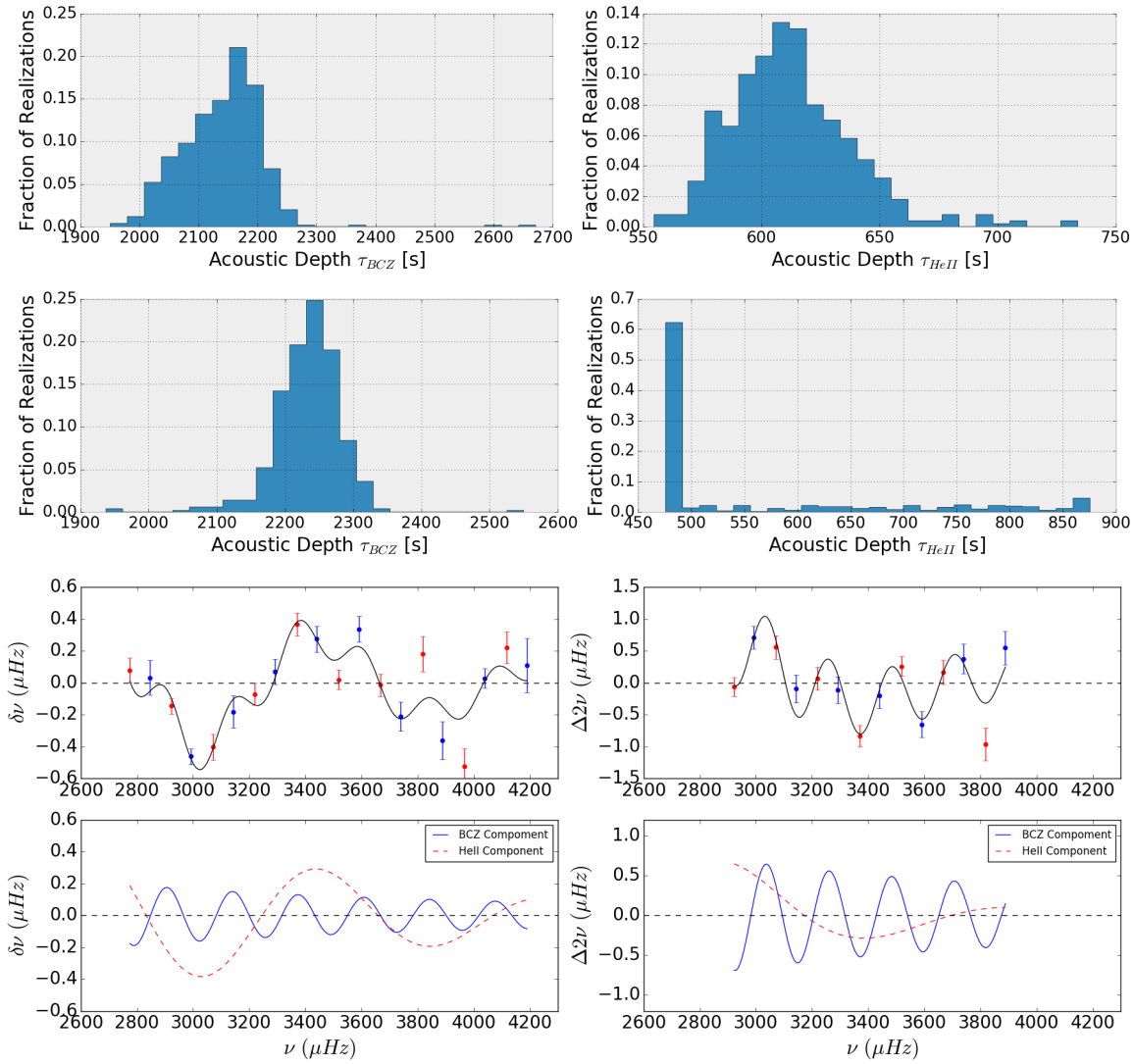

Figure C.1: Histograms of the results for the frequencies (top) and second differences (middle) and fit of both methods (bottom) for star KIC008006161.

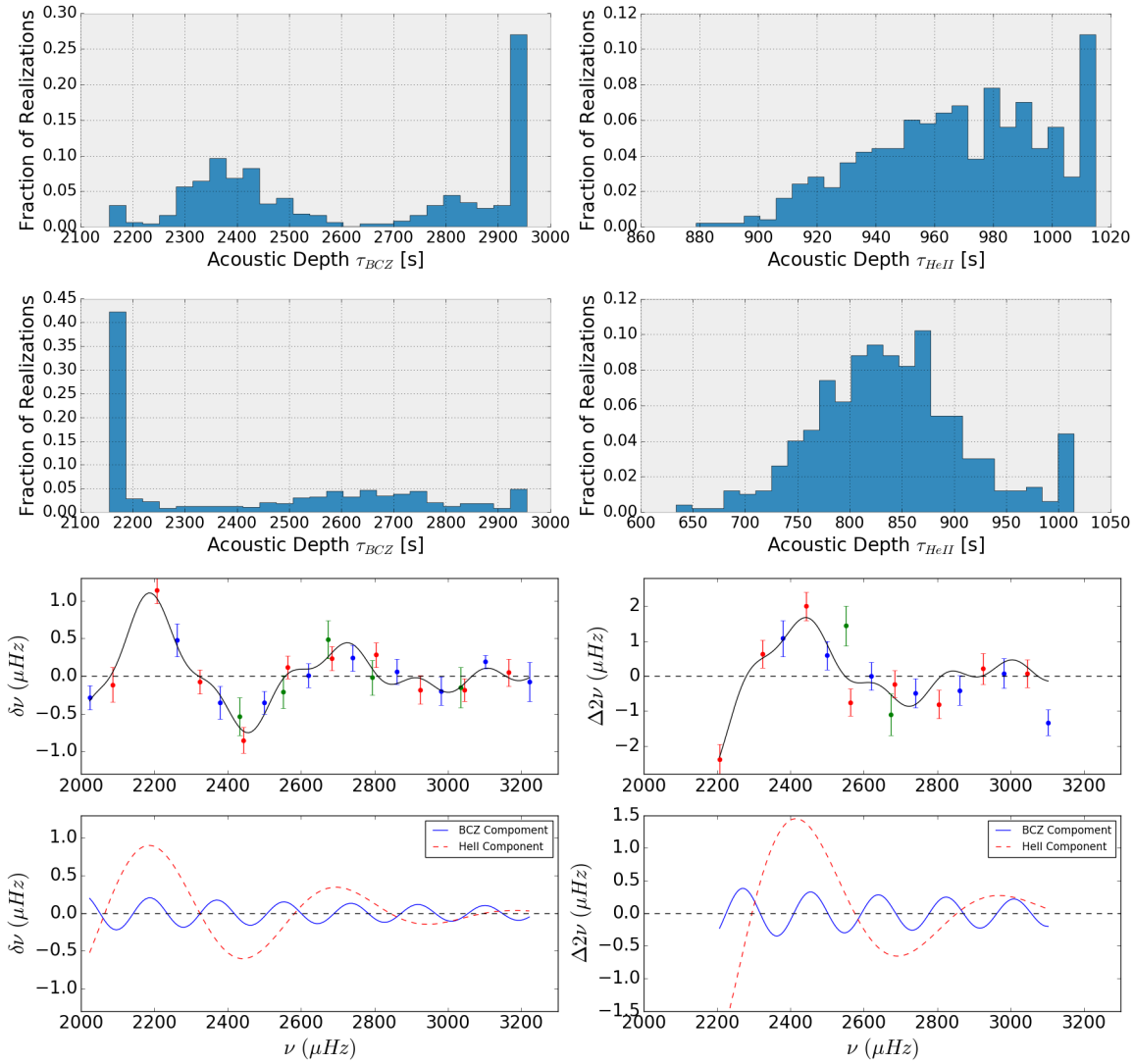

Figure C.2: Histograms of the results for the frequencies (top) and second differences (middle) and fit of both methods (bottom) for star KIC008379927.

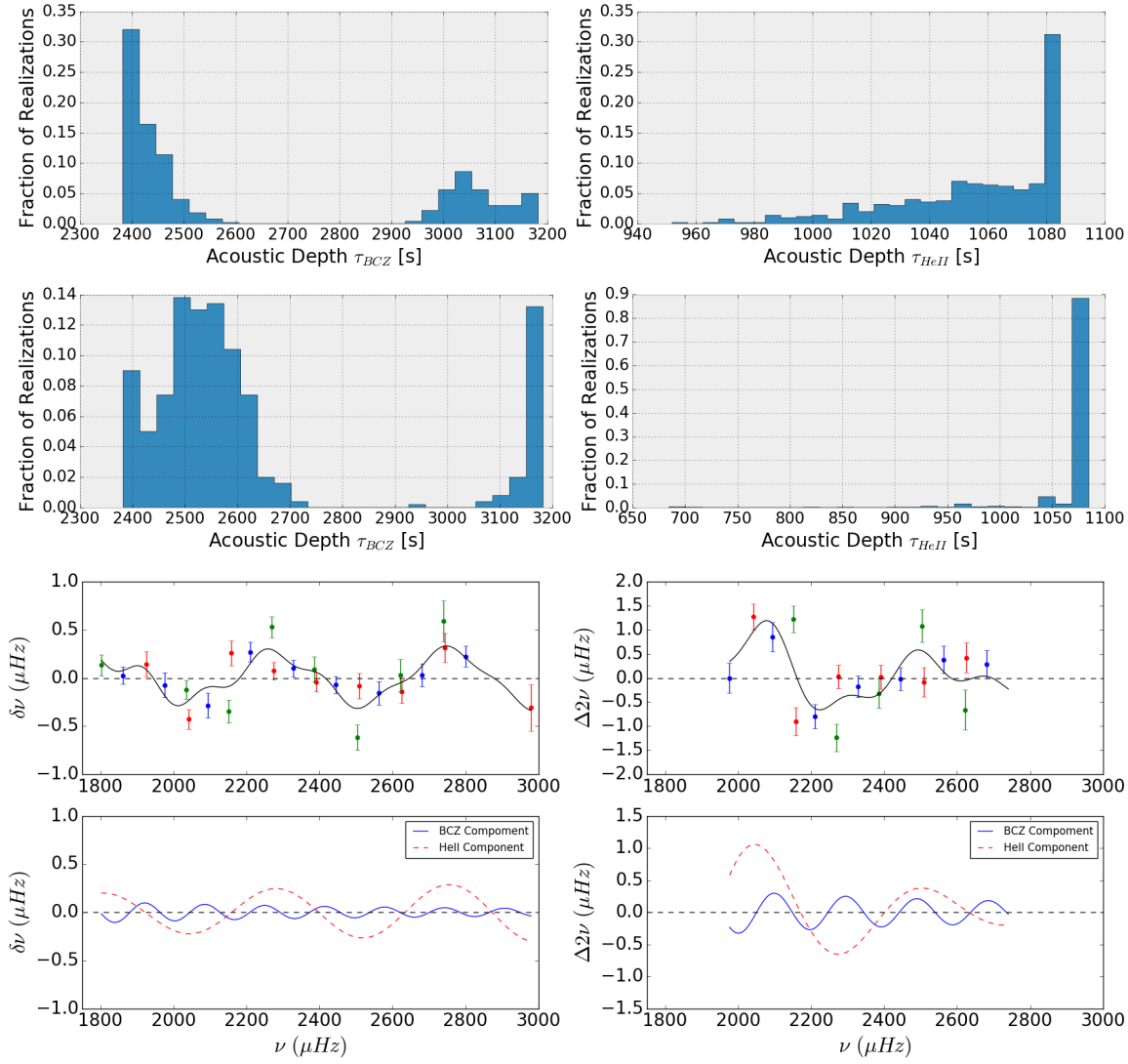

Figure C.3: Histograms of the results for the frequencies (top) and second differences (middle) and fit of both methods (bottom) for star KIC008760414.

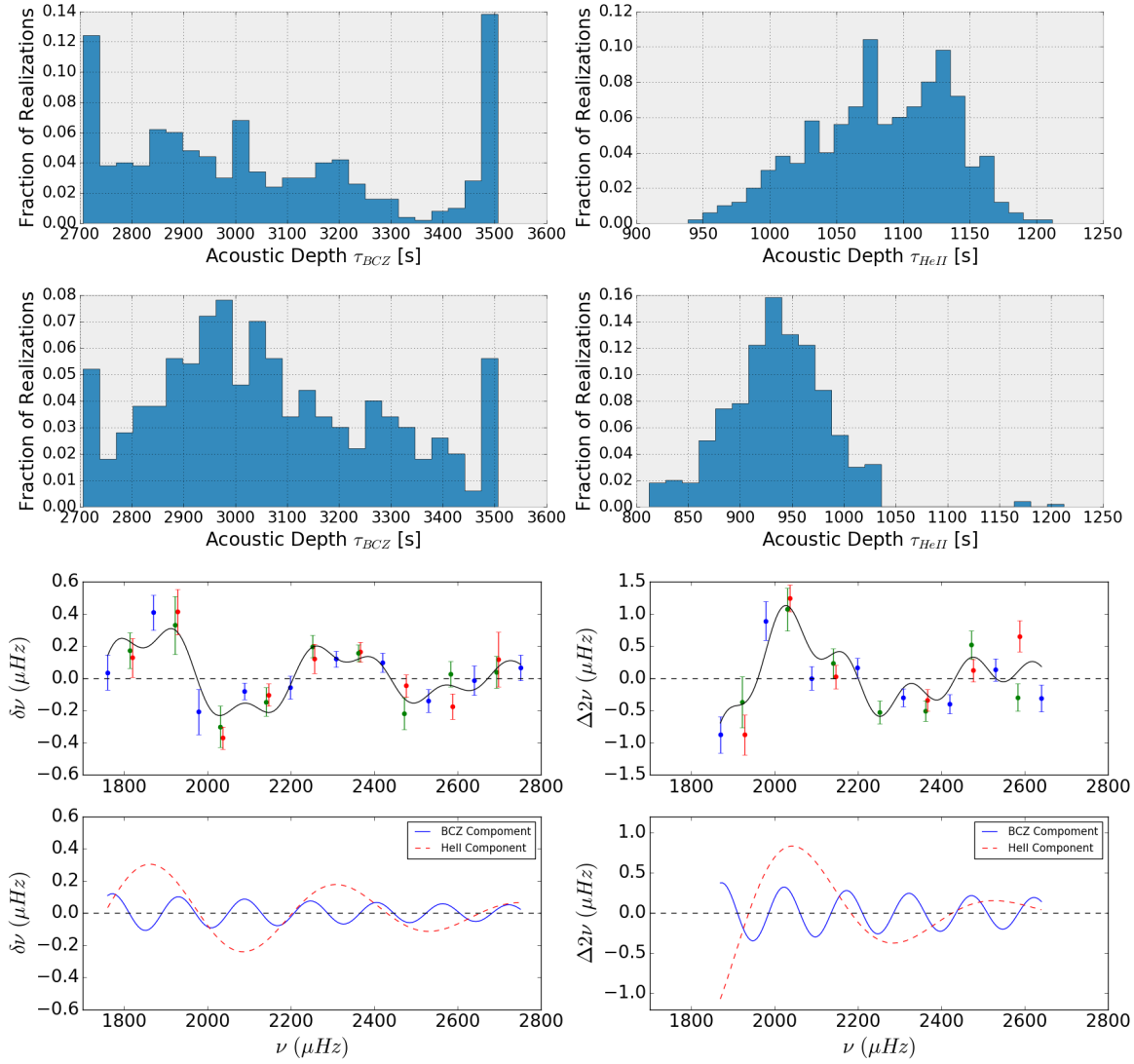

Figure C.4: Histograms of the results for the frequencies (top) and second differences (middle) and fit of both methods (bottom) for star KIC006603624.

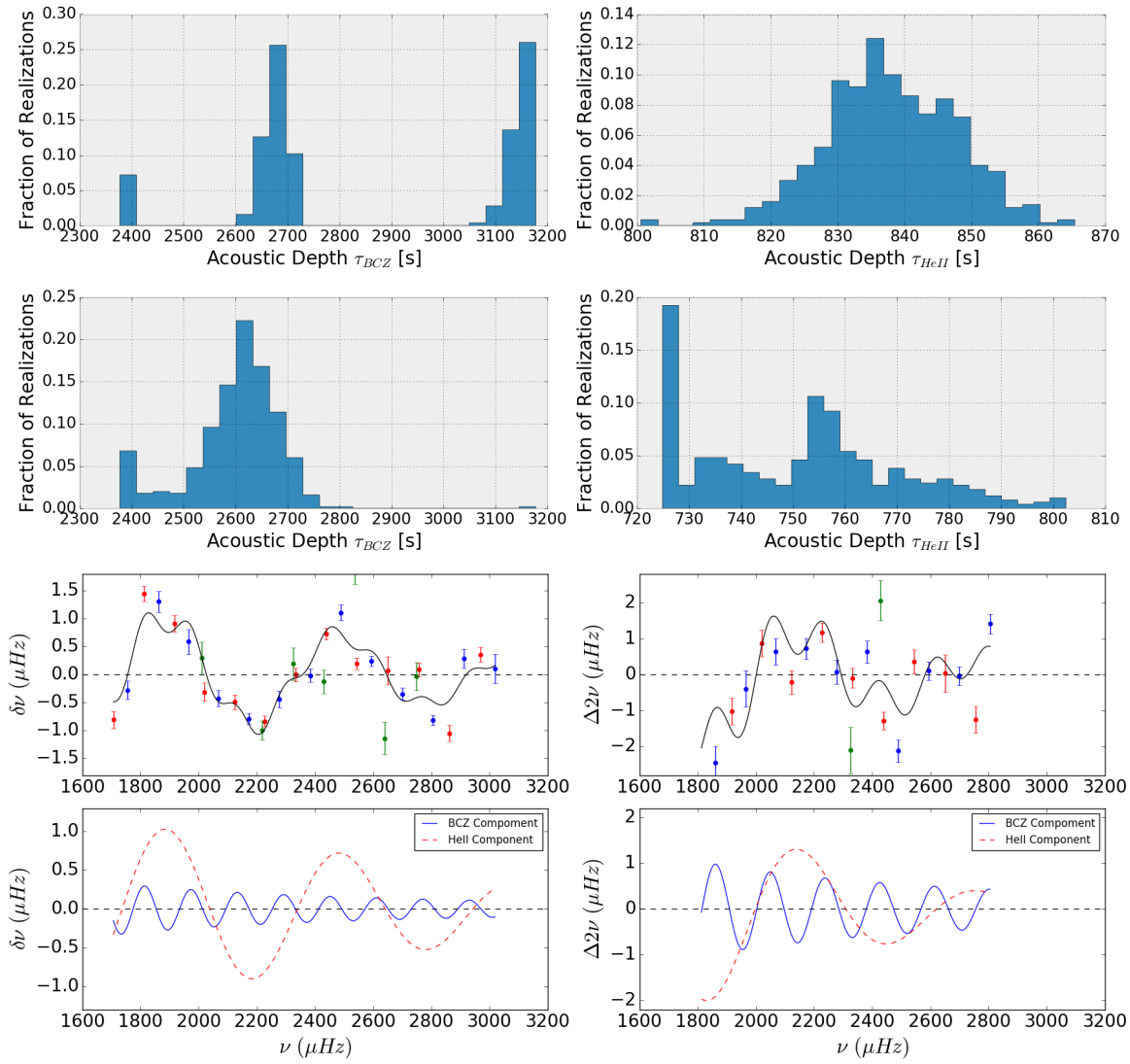

Figure C.5: Histograms of the results for the frequencies (top) and second differences (middle) and fit of both methods (bottom) for star KIC010454113.

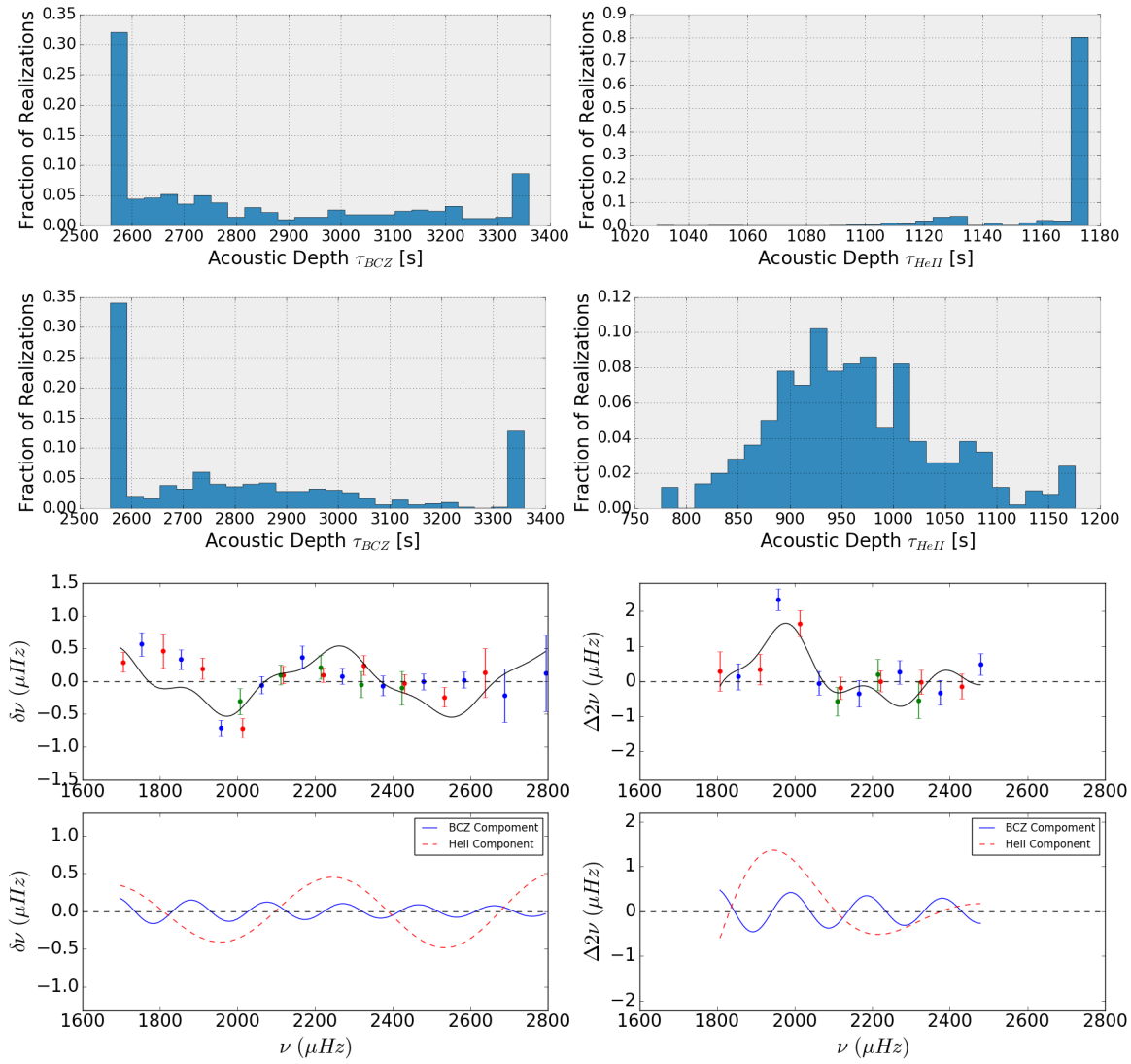

Figure C.6: Histograms of the results for the frequencies (top) and second differences (middle) and fit of both methods (bottom) for star KIC006106415.

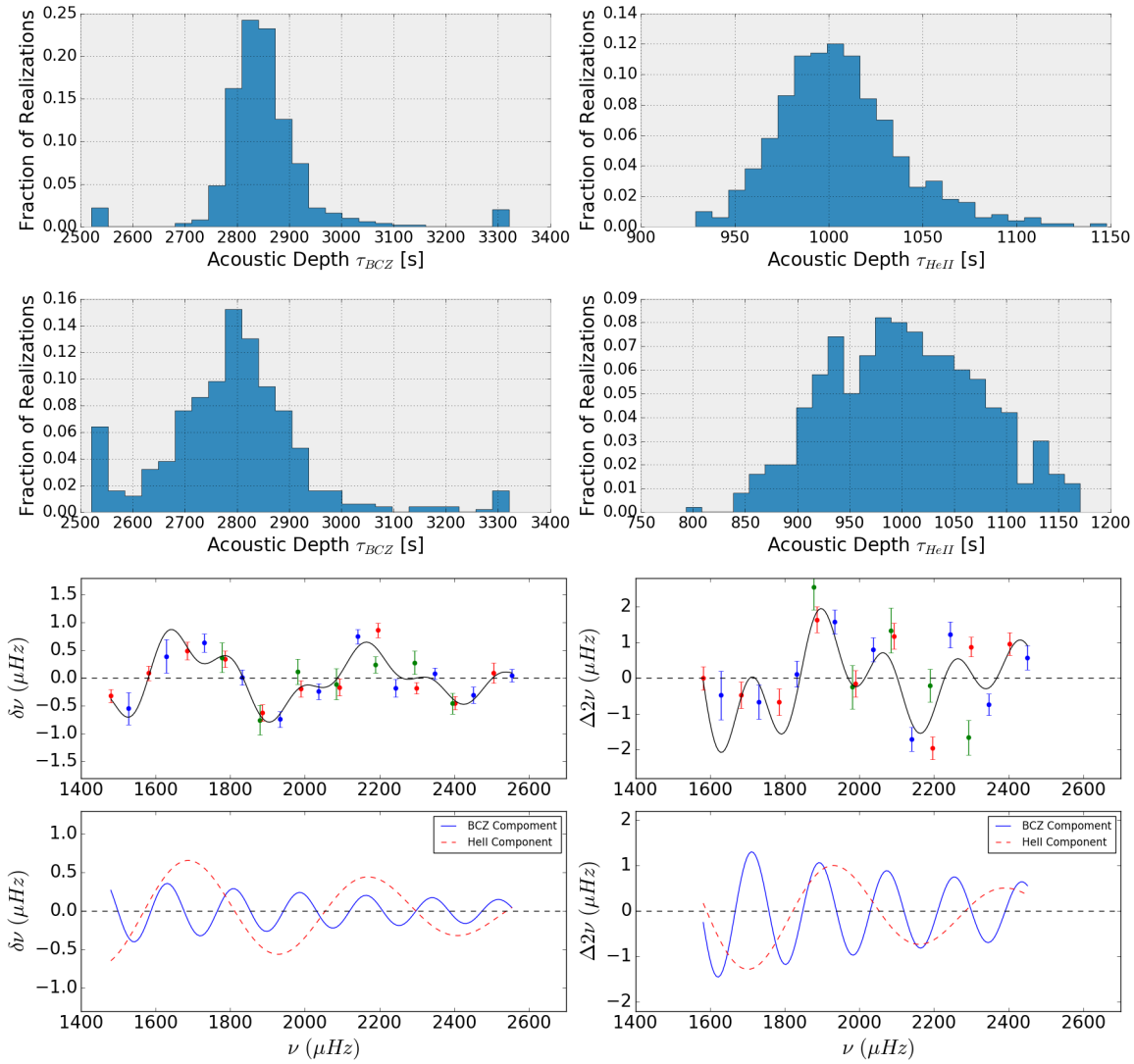

Figure C.7: Histograms of the results for the frequencies (top) and second differences (middle) and fit of both methods (bottom) for star KIC010963065.

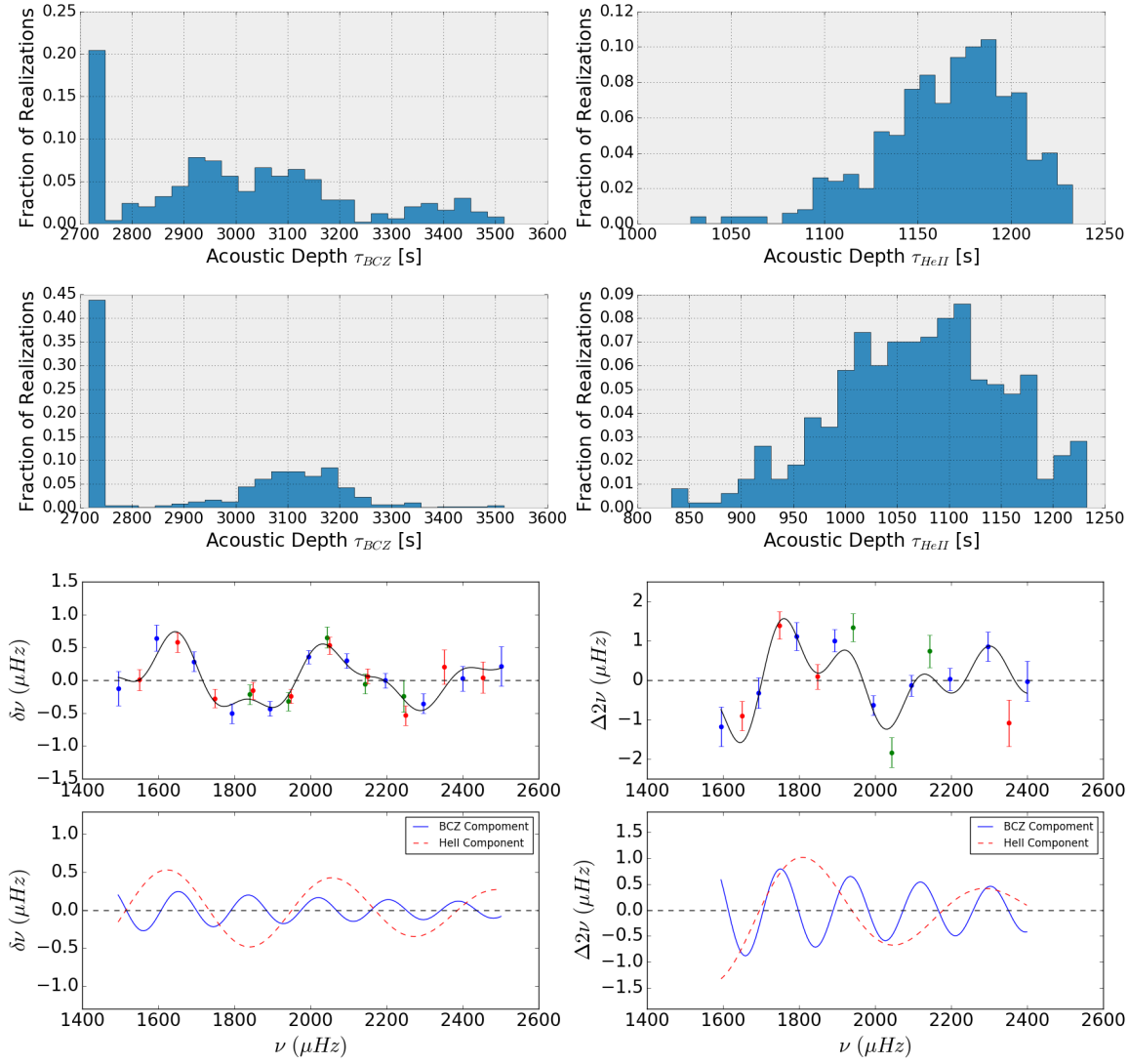

Figure C.8: Histograms of the results for the frequencies (top) and second differences (middle) and fit of both methods (bottom) for star KIC006116048.

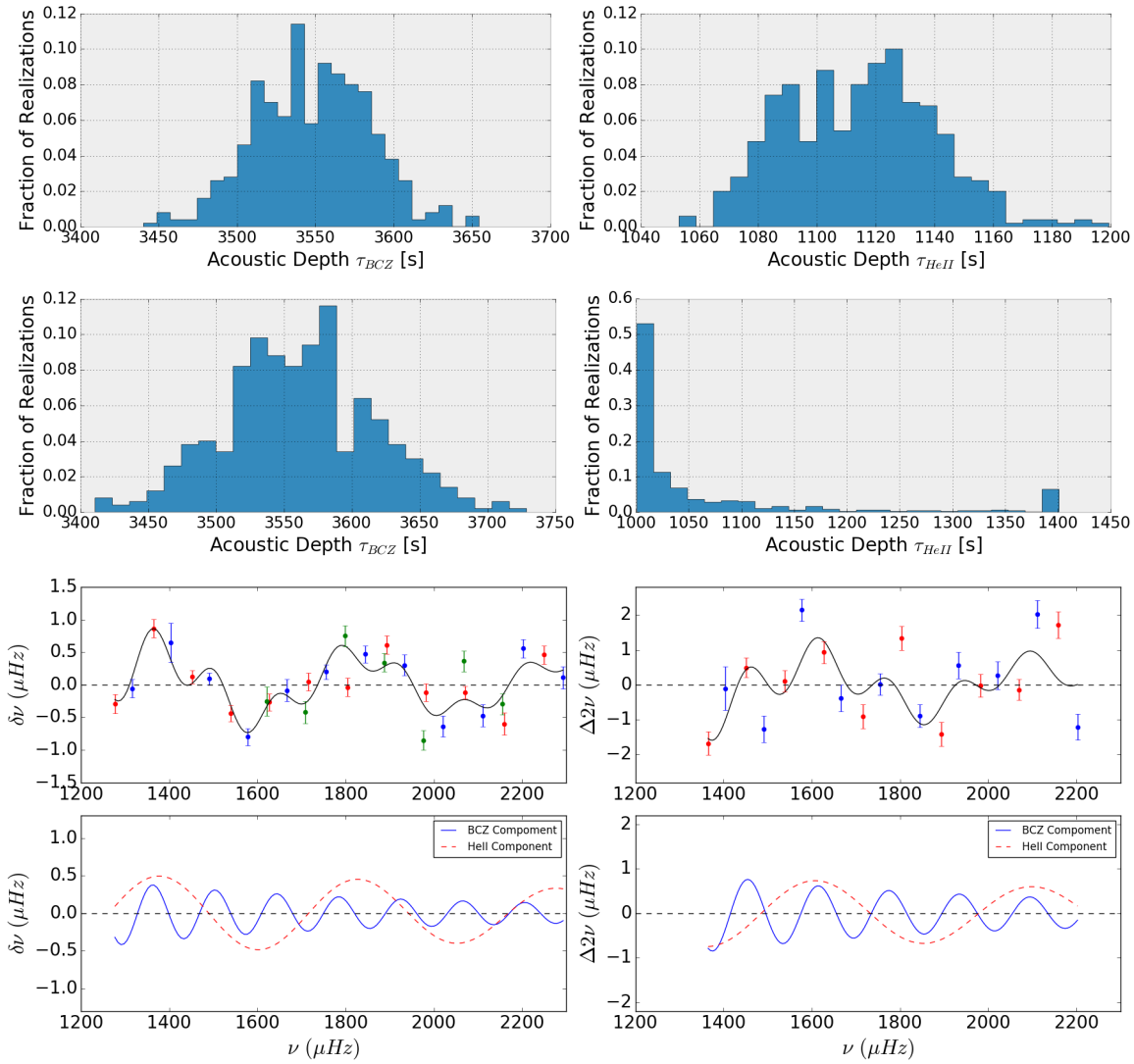

Figure C.9: Histograms of the results for the frequencies (top) and second differences (middle) and fit of both methods (bottom) for star KIC004914923.

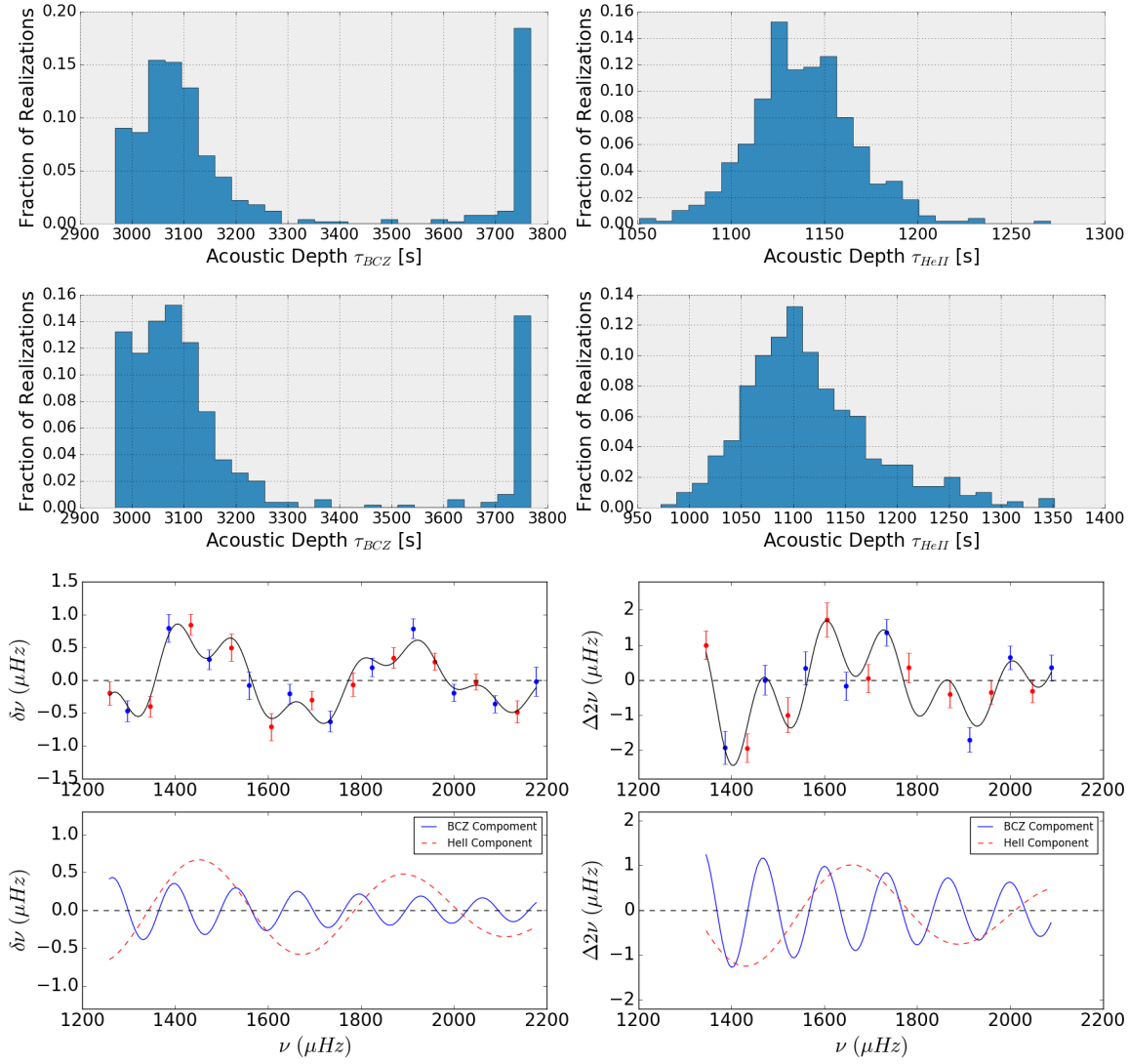

Figure C.10: Histograms of the results for the frequencies (top) and second differences (middle) and fit of both methods (bottom) for star KIC012009504.

Bibliography

Aerts, C., Christensen-Dalsgaard, J., and Kurtz, D. (2010). *Asteroseismology*. Astronomy and Astrophysics Library. Springer Netherlands. (Cited in: iii, 1, 10)

Basu, S., Chaplin, W. J., and Elsworth, Y. (2010). Determination of Stellar Radii from Asteroseismic Data. ApJ, 710:1596–1609. (Cited in: 38)

Bouchy, F. and Carrier, F. (2002). The acoustic spectrum of alpha Cen A. A&A, 390:205–212. (Cited in: iii, 3)

Broomhall, A.-M., Chaplin, W. J., Davies, G. R., Elsworth, Y., Fletcher, S. T., Hale, S. J., Miller, B., and New, R. (2009). Definitive sun-as-a-star p-mode frequencies: 23 years of bison observations. MNRAS, 396:L100–L104. (Cited in: 25)

Bruntt, H., Basu, S., Smalley, B., Chaplin, W. J., Verner, G. A., Bedding, T. R., Catala, C., Gazzano, J.-C., Molenda-Żakowicz, J., Thygesen, A. O., Uytterhoeven, K., Hekker, S., Huber, D., Karoff, C., Mathur, S., Mosser, B., Appourchaux, T., Campante, T. L., Elsworth, Y., García, R. A., Handberg, R., Metcalfe, T. S., Quirion, P.-O., Régulo, C., Roxburgh, I. W., Stello, D., Christensen-Dalsgaard, J., Kawaler, S. D., Kjeldsen, H., Morris, R. L., Quintana, E. V., and Sanderfer, D. T. (2012). Accurate fundamental parameters and detailed abundance patterns from spectroscopy of 93 solar-type Kepler targets. MNRAS, 423:122–131. (Cited in: 38)

Charbonneau, P. (1995). Genetic Algorithms in Astronomy and Astrophysics. ApJS, 101:309. (Cited in: 22)

Christensen-Dalsgaard, J., Monteiro, M. J. P. F. G., and Thompson, M. J. (1995). Helioseismic estimation of convective overshoot in the Sun. MNRAS, 276. (Cited in: 14)

Christensen-Dalsgaard, J. and Perez Hernandez, F. (1992). The phase function for stellar acoustic oscillations. I - Theory. MNRAS, 257:62–88. (Cited in: 11)

Cowling, T. G. (1941). The non-radial oscillations of polytropic stars. MNRAS, 101:367. (Cited in: 9)

Cox, J. (1980). *Theory of Stellar Pulsation*. Princeton series in astrophysics. Princeton University Press. (Cited in: 8)

Deubner, F.-L. and Gough, D. (1984). Helioseismology: Oscillations as a Daignostic of the Solar Interior. ARA&A, 22:593–619. (Cited in: 9)

Eddington, A. S. (1988). *The Internal Constitution of the Stars*. Cambridge Science Classics. Cambridge University Press. (Cited in: 1)

Faria, J. P. (2013). Asteroseismology of 16 cyg a and b. Master's thesis. (Cited in: v, 3, 4, 22, 33, 34, 43, 52)

Gough, D. O. (1990). Comments on Helioseismic Inference. In Osaki, Y. and Shibahashi, H., editors, *Progress of Seismology of the Sun and Stars*, volume 367 of *Lecture Notes in Physics, Berlin Springer Verlag*, page 283. (Cited in: 2)

Gough, D. O. and Thompson, M. J. (1988). Magnetic Perturbations to Stellar Oscillation Eigenfrequencies. In Christensen-Dalsgaard, J. and Frandsen, S., editors, *Advances in Helio- and Asteroseismology*, volume 123 of *IAU Symposium*, page 155. (Cited in: 2)

Houdek, G. and Gough, D. O. (2007). An asteroseismic signature of helium ionization. MNRAS, 375:861–880. (Cited in: 3, 12, 18, 43, 44)

Marques, J. P., Monteiro, M. J. P. F. G., and Fernandes, J. M. (2008). Grids of stellar evolution models for asteroseismology (cesam + posc). Ap&SS, 316:173–178. (Cited in: v, 29, 34)

Mazumdar, A., Monteiro, M. J. P. F. G., Ballot, J., Antia, H. M., Basu, S., Houdek, G., Mathur, S., Cunha, M. S., Silva Aguirre, V., García, R. A., Salabert, D., Verner, G. A., Christensen-Dalsgaard, J., Metcalfe, T. S., and Chaplin, W. J. (2012). Acoustic glitches in solar-type stars from Kepler. *Astronomische Nachrichten*, 333:1040–1043. (Cited in: 4)

Mazumdar, A., Monteiro, M. J. P. F. G., Ballot, J., Antia, H. M., Basu, S., Houdek, G., Mathur, S., Cunha, M. S., Silva Aguirre, V., García, R. A., Salabert, D., Verner, G. A., Christensen-Dalsgaard, J., Metcalfe, T. S., Sanderfer, D. T., Seader, S. E., Smith, J. C., and Chaplin, W. J. (2014). Measurement of Acoustic Glitches in Solar-type Stars from Oscillation Frequencies Observed by Kepler. ApJ, 782:18. (Cited in: vi, 3, 18, 33, 38, 39, 43, 44, 57)

Monteiro, M. J. P. F. G. (2008). Porto Oscillation Code (posc). Ap&SS, 316:121–127. (Cited in: 29)

Monteiro, M. J. P. F. G., Christensen-Dalsgaard, J., and Thompson, M. J. (1994). Seismic study of overshoot at the base of the solar convective envelope. A&A, 283:247–262. (Cited in: 2, 4, 14, 18, 22, 43)

Monteiro, M. J. P. F. G., Christensen-Dalsgaard, J., and Thompson, M. J. (2000). Seismic study of stellar convective regions: the base of the convective envelope in low-mass stars. MNRAS, 316:165–172. (Cited in: 3)

Monteiro, M. J. P. F. G. and Thompson, M. J. (2005). Seismic analysis of the second ionization region of helium in the Sun - I. Sensitivity study and methodology. MNRAS, 361:1187–1196. (Cited in: iv, 2, 4, 16, 18, 43)

Morel, P. and Lebreton, Y. (2008). CESAM: a free code for stellar evolution calculations. Ap&SS, 316:61–73. (Cited in: vi, 29, 39)

Schuler, S. C., Cunha, K., Smith, V. V., Ghezzi, L., King, J. R., Deliyannis, C. P., and Boesgaard, A. M. (2011). Detailed Abundances of the Solar Twins 16 Cygni A and B: Constraining Planet Formation Models. ApJ, 737:L32. (Cited in: 33)

Unno, W., Osaki, Y., Ando, H., Saio, H., and Shibahashi, H. (1989). *Nonradial oscillations of stars*. (Cited in: 8)

Verma, K., Faria, J. P., Antia, H. M., Basu, S., Mazumdar, A., Monteiro, M. J. P. F. G., Appourchaux, T., Chaplin, W. J., García, R. A., and Metcalfe, T. S. (2014). Asteroseismic Estimate of Helium Abundance of a Solar Analog Binary System. ApJ, 790:138. (Cited in: 33, 34, 37)

Vorontsov, S. V. (1988). A Search of the Effects of Magnetic Field in the Solar 5-MINUTE Oscillations. In Christensen-Dalsgaard, J. and Frandsen, S., editors, *Advances in Helio- and Asteroseismology*, volume 123 of *IAU Symposium*, page 151. (Cited in: 2)

White, T. R., Huber, D., Maestro, V., Bedding, T. R., Ireland, M. J., Baron, F., Boyajian, T. S., Che, X., Monnier, J. D., Pope, B. J. S., Roettenbacher, R. M., Stello, D., Tuthill, P. G., Farrington, C. D., Goldfinger, P. J., McAlister, H. A., Schaefer, G. H., Sturmann, J., Sturmann, L., ten Brummelaar, T. A., and Turner, N. H. (2013). Interferometric radii of bright Kepler stars with the CHARA Array: Theta Cygni and 16 Cygni A and B. MNRAS, 433:1262–1270. (Cited in: 33)